Bioorganic Chemistry 91 (2019) 103125

Contents lists available at ScienceDirect

Bioorganic Chemistry

journal homepage: www.elsevier.com/locate/bioorg

Searching new structural scaffolds for BRAF inhibitors. An integrative study using theoretical and experimental techniques

Ludmila E. Campos[a,b], Francisco M. Garibotto[a,b], Emilio Angelina[c], Jiri Kos[d], Tihomir Tomašič[e], Nace Zidar[e], Danijel Kikelj[e], Tomas Gonec[f], Pavlina Marvanova[f], Petr Mokry[f], Josef Jampilek[d,g], Sergio E. Alvarez[a,b,*], Ricardo D. Enriz[a,b,*]

[a] *Facultad de Química, Bioquímica y Farmacia, Universidad Nacional de San Luis, Ejército de los Andes 950, 5700 San Luis, Argentina*
[b] *Instituto Multidisciplinario de Investigaciones Biológicas (IMIBIO-SL), Ejército de los Andes 950, 5700 San Luis, Argentina*
[c] *Laboratorio de Estructura Molecular y Propiedades, Área de Química Física, Departamento de Química, Facultad de Ciencias Exactas y Naturales y Agrimensura, Universidad Nacional del Nordeste, Avda. Libertad 5460, 3400 Corrientes, Argentina*
[d] *Division of Biologically Active Complexes and Molecular Magnets, Regional Centre of Advanced Technologies and Materials, Faculty of Science, Palacky University Olomouc, Slechtitelu 27, 78371 Olomouc, Czech Republic*
[e] *University of Ljubljana, Faculty of Pharmacy, Aškerčeva 7, 1000 Ljubljana, Slovenia*
[f] *Department of Chemical Drugs, Faculty of Pharmacy, University of Veterinary and Pharmaceutical Sciences Brno, Palackeho 1, 61242 Brno, Czech Republic*
[g] *Department of Analytical Chemistry, Faculty of Natural Sciences, Comenius University, Ilkovicova 6, 84215 Bratislava, Slovakia*

ARTICLE INFO

Keywords:
BRAF inhibitors
Virtual screening
Synthesis
Bioassays
Molecular modeling

ABSTRACT

The identification of the V600E activating mutation in the protein kinase **BRAF** in around 50% of melanoma patients has driven the development of highly potent small inhibitors (BRAFi) of the mutated protein. To date, Dabrafenib and Vemurafenib, two specific BRAFi, have been clinically approved for the treatment of metastatic melanoma. Unfortunately, after the initial response, tumors become resistant and patients develop a progressive and lethal disease, making imperative the development of new therapeutic options. The main objective of this work was to find new BRAF inhibitors with different structural scaffolds than those of the known inhibitors. Our study was carried out in different stages; in the first step we performed a virtual screening that allowed us to identify potential new inhibitors. In the second step, we synthesized and tested the inhibitory activity of the novel compounds founded. Finally, we conducted a molecular modelling study that allowed us to understand interactions at the molecular level that stabilize the formation of the different molecular complexes.

Our theoretical and experimental study allowed the identification of four new structural scaffolds, which could be used as starting structures for the design and development of new inhibitors of BRAF. Our experimental data indicate that the most active compounds reduced significantly ERK½ phosphorylation, a measure of BRAF inhibition, and cell viability. Thus, from our theoretical and experimental results, we propose new substituted hydroxynaphthalenecarboxamides, *N*-(hetero)aryl-piperazinylhydroxyalkylphenylcarbamates, substituted piperazinylethanols and substituted piperazinylpropandiols as initial structures for the development of new inhibitors for BRAF. Moreover, by performing QTAIM analysis, we are able to describe in detail the molecular interactions that stabilize the different Ligand-Receptor complexes. Such analysis indicates which portion of the different molecules must be changed in order to obtain an increase in the binding affinity of these new ligands.

1. Introduction

The BRAF/MEK½/ERK½ cascade is one of the major pathways deregulated in many types of cancer. Oncogenic mutations in BRAF occur in around 50% of melanoma patients but also in colon adenocarcinoma (5–12%), papillary thyroid carcinoma (39–69%), and others [1,2]. Upon activation of this pathway, BRAF phosphorylates and activates the dual kinase MEK½, which in turn phosphorylates and activates its only target ERK ½ at Tyr 204/187 and Thr202/185 residues. RAF family includes 3 members: ARAF, BRAF and CRAF, although oncogenic mutations occur mostly in BRAF gene. The majority of BRAF mutations consist in substitutions of valine for glutamic acid

---

* Corresponding authors at: Facultad de Química, Bioquímica y Farmacia, Universidad Nacional de San Luis and Instituto Multidisciplinario de Investigaciones Biológicas (IMIBIO-SL CONICET), Ejército de los Andes 950, 5700 San Luis, Argentina.
E-mail addresses: sealvarez98@gmail.com, sealvar@unsl.edu.ar (S.E. Alvarez), denriz@unsl.edu.ar (R.D. Enriz).

https://doi.org/10.1016/j.bioorg.2019.103125
Received 10 April 2019; Received in revised form 4 July 2019; Accepted 11 July 2019

($BRAF^{V600E}$), or less frequently for lysine ($BRAF^{V600K}$), at position 600 leading to a constitutive active protein that does not require external stimuli to be activated [1–3]. To date, the U.S. Food and Drugs Administration have approved the use of two BRAF inhibitors (BRAFi), Vemurafenib [4] and Dabrafenib [5], and two MEK inhibitors (MEKi), trametinib and cobimetinib [6,7], for the treatment of metastatic melanoma. BRAFi and MEKi constitute the first-line treatment for $BRAF^{V600E}$ mutated melanomas, however the development of acquired resistance invariably occurs, and in some cases no clinical benefit at all is observed [8,9]. Although many mechanisms of resistance have been reported, most of them involve the reactivation of ERK½ signaling [10–12]. Moreover, BRAFi therapy also induces paradoxical activation of ERK signaling in $BRAF^{wt}$ tissue [13] that may promote the formation of benign tumors in the skin [14]. Resistance development and secondary effects to BRAFi therapy reduce the effectiveness and durability of the clinical response, and justify the search and design of new potential BRAFi.

The high sequence conservation within the large family of protein kinases makes it difficult to develop selective inhibitors for a particular member of the family. Furthermore, nearly all of the approved protein kinase antagonists are steady-state competitive enzyme inhibitors of ATP and they interact with the ATP-binding pocket which is well conserved among the family of protein kinases [15]. However, protein kinases have high plasticity and it is well known that kinase conformational state has a great impact in inhibitor potency and selectivity [16]. Therefore, conformational plasticity of kinases can be exploited to design inhibitors that target a specific kinase type in a particular conformational state.

BRAF has an active site (including the so called catalytic loop) to which both ATP and inhibitors bind. The conserved DFG triad shifts to an ‘out’ conformation where the phenylalanine side chain vacates a lipophilic “allosteric” pocket that is available to inhibitor binding (i.e. DFG-out conformation). Compounds that bind to kinase in DFG-out state are classified as type II inhibitors [17], in contrast to the active DFG-in conformation. In the latter case, PHE is flipped toward the allosteric pocket and inhibitors that target this conformation (Type I inhibitors) bind at the ATP site but do not penetrate the allosteric pocket and therefore do not depend on specific kinase conformations for binding. There is a small set of kinases including BRAF that achieves a peculiar variant of the DFG-in conformation in which a conserved salt bridge between a glutamate in αC-helix and a lysine in the β3-sheet is broken. The disruption of this salt bridge causes an outward movement of the αC-helix (αC-helix-out) and renders the kinase in an inactive state despite the DFG triad residing in the ‘in’ conformation. Inhibitors that target the DFG-in αC-helix-out conformation are classified as type IIB while inhibitors that bind to the more typical inactive kinase conformation DFG-out are re-classified as type IIA inhibitors. Since only few kinases are able to perform this DFG-in, αC-helix-out conformation, inhibitors designed to target this particular kinase state have exhibited excellent selectivity towards the RAF kinase family. These inhibitors accommodate a propyl group in a small lipophilic pocket formed by the outward movement of αC-helix-out [18]. Vemurafenib is an example of a selective BRAF inhibitor that targets this kinase conformation.

Considering the important role of BRAF in processes related to cancer [1] and vemurafenib clinical limitations, the main objective of this work was to develop new inhibitors possessing different structural scaffolds than those of the already known inhibitors. Our study has been carried out in different stages; in the first step we performed a virtual screening that allowed us to identify potential new inhibitors. In the second step, we synthesized and tested the inhibitory activity of the novel compounds. Finally, we conducted a molecular modeling study that allowed us to understand interactions at the molecular level that stabilize the formation of the different molecular complexes. Fig. 1 shows an scheme of the various steps that have been carried out in this study.

2. Results and discussion

2.1. Structure-based approach to prioritize novel scaffolds as BRAF inhibitors

At the time we started this work, there were around 60 BRAF crystal structures available in the Protein Data Bank (PDB). Taking advantage of this structural information we pursued a structure-based drug design project searching for novel scaffolds that may function as BRAF inhibitors.

Structure-Based Virtual Screening (SBVS) strategies rely on the three dimensional structure of a target and on the ability of docking algorithms to predict the binding mode and the binding affinities of different compounds obtained from libraries.

As was previously remarked, protein kinases have high plasticity and several conformations, and it is well known that kinase conformational state has a great impact in inhibitor potency and selectivity [16]. BRAF crystal structures deposited in the PDB up to date cover the three more relevant kinase conformational states.

Fig. 2 shows superposition of BRAF in two of its conformational states, DFG-out (gray) and DFG-in αC-helix-out (cyan). In Fig. 2a, a type IIA inhibitor (gray sticks) accommodates a bulky aromatic group into the lipophilic pocket of DFG-out conformation (depicted as a gray surface) which is otherwise occluded in DFG-in like conformations. Thus, type IIA inhibitors that were designed to target the lipophilic pocket in DFG-out conformation would not bind properly at DFG-in conformations.

In contrast, in Fig. 2b, a type IIB inhibitor (cyan sticks) accommodates a small aliphatic group into a small lipophilic pocket created by the outward shift of αC-helix which disrupt the salt bridge between K483 and E501; such place can be occupied by the inhibitor in the DFG-in αC-helix-out conformation. This small but deep pocket is generally absent in DFG-in and DFG-out conformations in which the salt bridge holds αC-helix and β3-sheet together. Therefore, in order to allow more structural variety among selected compounds, virtual screening libraries should be docked against representative structures from each of the BRAF conformational states (ensemble docking). In other words, if only one of the BRAF conformations are considered in docking calculations, we could fish inhibitors targeting that conformation but we would miss inhibitors that stabilize other relevant BRAF conformations.

2.1.1. Virtual screening and docking power assessment

The docking process is usually divided into two major steps: first, the correct placement of the ligand at the protein binding-site and second, the estimation of the ligand affinity by a scoring function [19]. Scoring functions launched with docking software are usually calibrated with structurally very diverse complexes because they are intended for general use in any bimolecular system of interest. In part because of their general nature, standard docking scoring functions often might fail either to recover ligand known binding affinities (scoring power) or poses (docking power) or might fail to rank ligands by their affinities (ranking power) or also recover known ligands from decoys libraries (screening power). Therefore, before undertaking the search for novel BRAF inhibitors, we considered it was prudent to perform a retrospective study with known BRAF inhibitors to evaluate performance of docking algorithm in our system of study.

Metrics employed to evaluate and tune docking performance depends on the intended use of docking programs. Docking, scoring, ranking or screening power can be tuned depending on the particular task and experimental information available. The scoring function optimal for the different tasks may have some overlap, although improvements in affinity prediction are not always related to improvements in the docking performance [20]. To test screening power we measured the ability of AutoDock4 [21] standard scoring function to retrieve BRAF inhibitors from a decoys library. The decoys library was

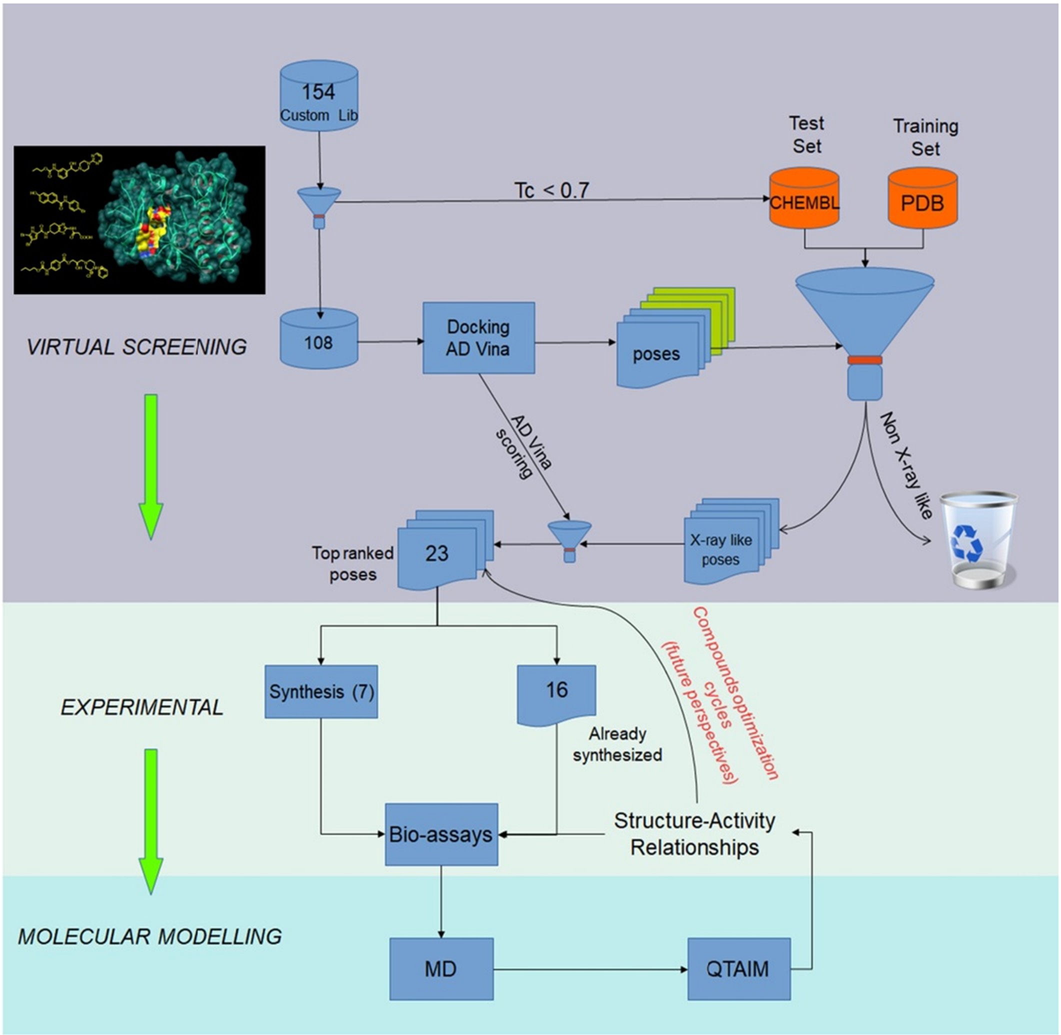

Fig. 1. Flow chart showing the various steps and techniques carried out in our study. The numbers inside the boxes indicate the number of compounds evaluated.

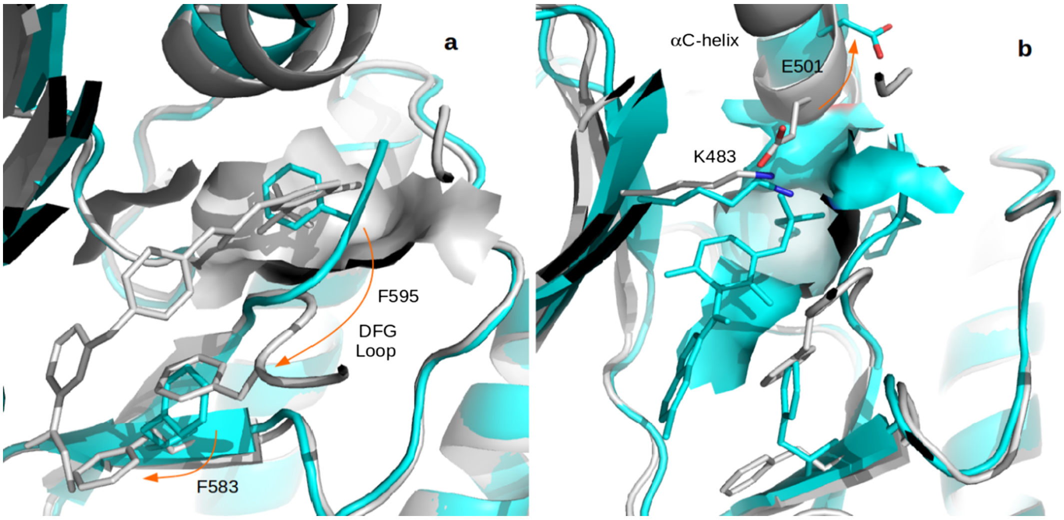

Fig. 2. Superposition of two conformations of BRAF (DFG-out is shown in grey color and DFG-in αC-helix-out in cyan)). Figure a: Transition from DFG-in to DFG-out conformation. Figure b: Type IIB inhibitor induce an outward shift of αC-helix.

compiled by seeding about 40 known BRAF inhibitors into a larger set of presumably non-binding compounds (decoys) that were automatically generated with the DUD-E server [22]. Decoy molecules have similar physical properties than actual ligands so that enrichment is not a mere separation by trivial physical characteristics, but are chemically distinct from ligands, so that they are likely to be non-binders.

BRAF inhibitors seeded into the decoys library were extracted from crystal structures of BRAF bound to inhibitors to later evaluate both

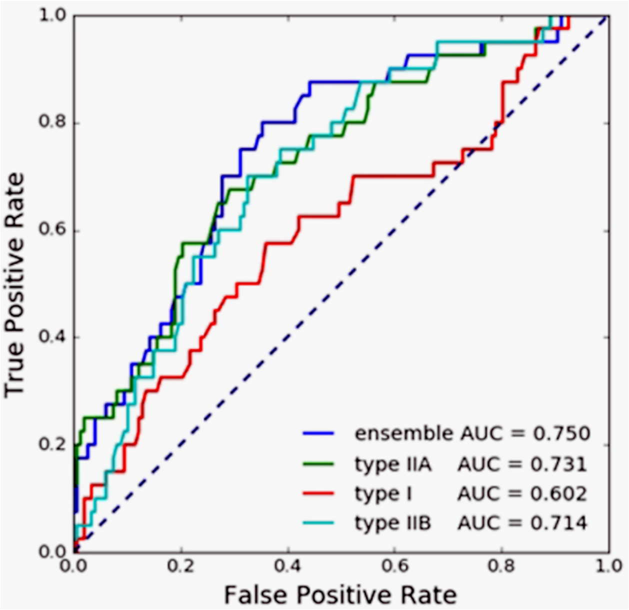

Fig. 3. Screening power evaluation of docking algorithms for retrieving known BRAF inhibitors from a decoys library.

docking power (i.e. by RMSD measurement) and screening power. Inhibitors were chosen considering that the three types of inhibitors are fairly represented within the inhibitors pool (i.e. types I, IIA and IIB are roughly in the same number). The decoy library was docked against a representative structure from each of the three most relevant BRAF conformational states, i.e. DFG-in, DFG-out and DFG-in αC-helix-out conformations. After docking the decoys library with AutoDock4, ROC (Receiver Operating Characteristic) curves were constructed and the Area Under the Curve (AUC) was computed. Fig. 3 depicts ROC curves and AUCs for virtual screening on each of the BRAF conformations as well as for the ensemble of BRAF conformations.

Ensemble docking helps to mitigate the lack of flexibility of docking receptor models by allowing docking a single ligand against multiple conformations of the protein and selecting the highest scoring binding mode from the ensemble of receptors. Any model with an AUC > 0.5 performs better than random in discriminating the most active compounds from less active ones. Unsurprisingly, the virtual screening (VS) prediction on the ensemble of BRAF conformations performs better than on single BRAF conformations (see AUCs in Fig. 3). This is in line with the fact that different types of BRAF inhibitors stabilize different conformations of the enzyme. As observed in the figure, the ensemble docking model performs reasonably well in the classification of the dataset (AUC ~ 0.75).

Moreover, since we know the experimental binding modes of the BRAF inhibitors in the decoys library we subsequently exploited that information to evaluate docking power, namely the ability of docking algorithm to predict the correct conformation of the ligand and placement in the receptor molecule (pose).

Docking power usually is evaluated by computing the root mean square deviation (RMSD) between the heavy atoms of the docked ligand and native crystal pose. Usually, a threshold of 2–3 Å RMSD is used to calculate the fraction of correct predictions.

Heat maps on Fig. 4a–c depict the RMSD values between crystallographic and docking poses of type IIA, type IIB and type I BRAF inhibitors, respectively. Each inhibitor was docked against the three relevant conformations of the enzyme and the conformation that achieves the best docking scoring is labeled with a green star.

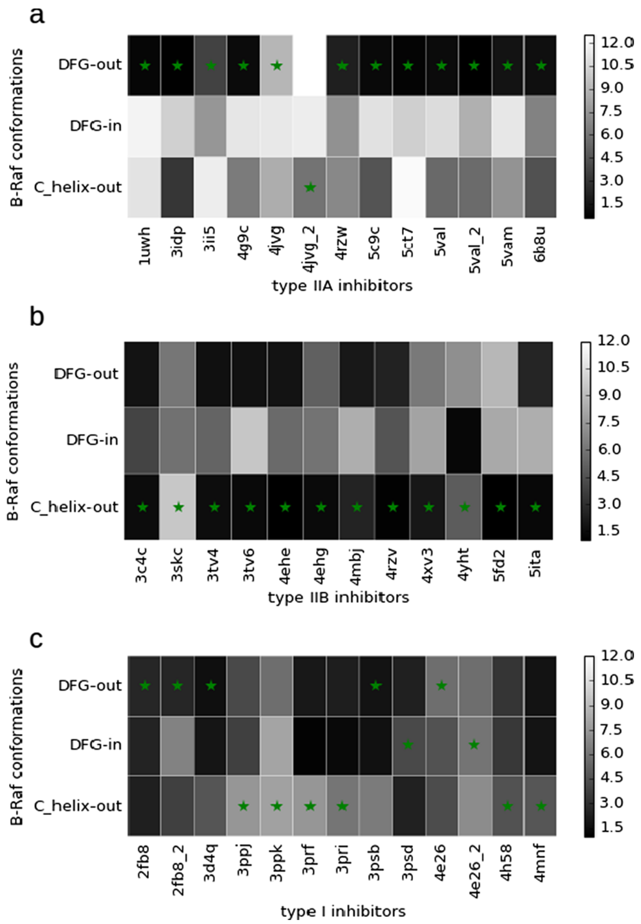

Fig. 4. Heat maps depicting RMSD differences between crystallographic and docking poses for type IIA (a), IIB (b) and type I (c) BRAF inhibitors as docked in the three relevant conformations of the enzyme. Best scoring conformation for each ligand is labeled with a green star. Ligands are named by the PDB ID of the BRAF native complex they belong to. Underscored PDB IDs represent different protonation states of the same ligand.

As depicted in Fig. 4a, Type IIA inhibitors can reproduce their crystallographic poses (i.e. considering a 2–3 Å RMSD tolerance) only when they are docked to the DFG-out conformation of BRAF. This makes sense because type IIA inhibitors were designed to target the allosteric pocket that is otherwise occluded in DFG-in conformations. There is also a good correspondence between docking power and scoring, namely enzyme conformation achieving the best pose for a particular ligand is also the one that show the best energy score, as indicated by the green stars in Fig. 4a. In practice, that means that prospective virtual screening campaigns will likely prioritize candidates that reproduce known inhibitors binding modes and therefore that have more chance of being true positives upon experimental corroboration.

Similarly, most of Type IIB inhibitors are docked correctly in their native-like BRAF conformation, DFG-in αC-helix-out. These inhibitors have a hydrophobic tail attached to a sulfonamide group and target a small hydrophobic pocket created between β3-sheet and αC-helix. In DFG-in conformation a conserved salt bridge between GLU501 and LYS483 holds together the αC-helix and the β3-sheet and prevent the formation of the small hydrophobic pocket between both segments. This explains why Type IIB inhibitors cannot dock properly to BRAF in the DFG-in conformation (see Fig. 4b). Regarding DFG-out state, several type IIB inhibitors bind to this conformation in a native-like pose because they can accommodate the small hydrophobic tail in the adjacent allosteric pocket characteristic to that conformation without a significant degradation in the RMSD value.

On the other hand, and unlike previous BRAF inhibitors types, several type I inhibitors bind better to DFG-out or DFG-in αC-helix-out BRAF conformations than to its own DFG-in conformation. Moreover, many of them cannot reproduce the crystallographic poses within a 2–3 Å RMSD tolerance in any of the BRAF conformations. Even though type I inhibitors do not perform as well as type IIA and IIB inhibitors, we consider that our proposed virtual screening protocol involving the three most relevant BRAF conformations performs well in terms of screening and docking power.

2.1.2. Pre-selection of candidate compounds and results of the virtual screening

Most kinase inhibitors discovered to date bind to kinase ATP binding cleft and roughly mimic the hydrogen bonds normally formed by the adenine, ribose and/or triphosphate moieties of ATP. Structure of ATP analog bound to kinase AKT1 (PDB code 1O6L) provides evidence about ATP binding mode at kinases ATP binding cleft. ATP binds in the cleft with the adenine ring forming hydrogen bonds with the kinase 'hinge', i.e. the segment that connects the amino- and carboxy-terminal kinase domains. The ribose and triphosphate groups enter in a tight channel and triphosphate moiety interacts with the activation segment that contains the common DFG motif, via two magnesium ions (PDB code 1O6L).

It is clear that the compounds selected for further testing should bear some structural resemblance to vemurafenib and other known ligands; i.e. part of the molecule mimicking adenine and other portion that mimics the triphosphate moiety. In addition some conformational flexibility could be convenient. Based on these considerations, we selected a group of 153 compounds including chalcones, acetogenins, protoberberines, nitrosopyrimidines, carbamates and carboxamides among others that already form part of our collection of compounds. We also include some new compounds (not reported yet) structurally related. The fingerprints of these 153 compounds were calculated using Open Babel [23], a chemical expert system mainly used for converting chemical file formats, and the results were compared with fingerprints obtained for the 40 compounds used previously to evaluate the docking "powers". Compounds that have a Tanimoto index (Tc) [19] greater than 0.7 were discarded. Note that the fingerprints are a way to encode the structure of a molecule in order to compare it with other compounds; whereas the Tc is a measure of the similarity between two structures ranging from 0 to 1. Based on Tc index, we selected 108 structurally diverse compounds which possess structural differences with respect to already-known BRAF inhibitors, justifying their further study. Each of the 108 compounds was docked against the three relevant conformations of the enzyme (ensemble docking). Then, the compounds were ranked according to the score achieved in the best enzyme conformation and the 30 top ranked compounds were selected. From these compounds, only the ones that bind in a pose that resemble the binding mode of known BRAF inhibitors like Vemurafenib (see below) were selected. Thus, 23 compounds were selected as potential inhibitors, while the remaining 7 were discarded because they unite in a different pose to that of the crystallized structures. All these 23 compounds have shown a better score when docked to the DFG-in αC-helix-out conformation of the enzyme, hence they were regarded as potential BRAF type IIB inhibitors.

2.2. Chemistry

Our model predicted 23 compounds as potential inhibitors of BRAF (Table 1). Those compounds were tested in an *in vitro* ERK1/2 phosphorylation assay as an indirect measure of BRAF inhibition in melanoma cells (results shown in the next section).

The compounds **1–8** were prepared by means of microwave-assisted synthesis in one step. Briefly, the carboxyl group was activated with phosphorus trichloride, and then aminolysis of acyl chloride by ring-substituted aniline in dry chlorobenzene yielded a final amide. All the compounds were purified by recrystallization from ethanol [24–26].

Synthesis and characterization of compounds **9–13** have been previously reported [27–30] (See *Suplemmentary Information)*. These compounds have been reported DNA gyrase inhibitors interacting with the ATP-binding site of the enzyme.

Reaction of 2- or 3- or 4-aminoacetophenone and a suitable alkyl chloroformiate gave alkyl (2-/3-/4-acetylphenyl)carbamates **14a–21a**, which reacted with bromine or with copper (II) bromide in chloroform/ethyl acetateto yield alkyl [2-/3-/4-(bromoacetyl)phenyl]carbamates **14b–21b**; these compounds by treatment with different *N*-mono-substituted aryl(heteroaryl)piperazines provided the corresponding alkyl {2-/3-/4-[(4-aryl(heteroaryl)piperazin-1-yl)acetyl]phenyl}carbamates **14c–21c**. Subsequent reduction of keto group using $NaBH_4$ provided target alkyl {2-/3-/4-[1-hydroxy-2-(4-aryl(heteroaryl)piperazin-1-yl)ethyl]phenyl}carbamates **14–21**, see Scheme 1.

Studied 1-(3-{4-[(alkoxycarbonyl)amino]benzoyloxy}-2-hydroxypropyl)-4-phenylpiperazin-1-ium chlorides **22** and **23** were prepared by multiple-step reaction described in Scheme 2. Epoxides **22a** and **23a** were prepared from 4-aminobenzoic acid through reaction with propyl and methylchloroformiates giving appropriate 4-[(alkoxycarbonyl)amino]benzoic acids. Chlorides of these acids formed by thionyl chloride treatment gave desired epoxides **22a** and **23a** after reaction with 2,3-epoxypropan-1-ol [31]. In the last step, final compounds **22** and **23** were prepared by a reaction of the epoxides with 1-(4-phenyl)piperazine and then converted to the hydrochloride salts using ethereal HCl to enhance their solubility in water [32].

2.3. Biological assays

Next, it was important to study whether or not these 23 compounds inhibit BRAF. Since the BRAF/MEK/ERK pathway is lineal, it is possible to relate the BRAF activity to the levels of phosphorylated ERK (pERK) in a western blot assay. Indeed, ERK½ kinase is the only substrate of MEK ½ that has been described to date [33]. To this end, Lu1205 melanoma cell line that express the mutant kinase $BRAF^{V600E}$, was employed. To establish the reliability of our model, we first tested the response of Lu1205 cells to the known $BRAF^{V600E}$ inhibitor Vemurafenib. In line with previous reports, we show here that Vemurafenib strongly reduced ERK phosphorylation at both 1 and 10 μM [34]. The effect of Vemurafenib is less pronounced after 48–72 h, probably indicating that ERK reactivation occurs, as was shown by other authors (Fig. 5) [35,36].

After determining that Lu1205 cells are responsive to Vemurafenib treatment as we expected and it is reported in literature, we considered that this cell model is appropriate for the following assays. Next, we evaluated the biological activity of the compounds listed in the Table 1. Since the goal of this study was to find new inhibitors of BRAF, we consider that 2 h treatment should be enough to show whether or not the new compounds have any noticeable activity. Thus, to perform a quick initial screening of BRAF kinase inhibition, we determined the phosphorylation of ERK in Lu1205 cells treated with the compounds at 10 μM for 2 h by In-Cell Western (ICW) or western blot (Fig. 6).

As shown in Fig. 6, compounds **1, 2, 9, 10, 19**–**22** reduced ERK phosphorylation by more than 30% and were selected to perform a more detailed study. Compounds **17, 18** and **23,** which did not show, or showed little inhibitory activity in the previous screening, were also included to verify the specificity of the compounds that did show activity. Next, Lu1205 cells were treated with the 11 selected compounds for 2 h at 10 and 1 μM. Remarkably, all the compounds selected reduce ERK phosphorylation at different magnitude indicating that they have BRAF inhibitory activity, although only compounds **1, 2, 9, 19, 20–22** and **23** reduced significantly pERK suggesting that they have a stronger inhibitory effect (Fig. 7). It is important to notice that, although some compounds (ie. compound 17) decreased ERK phosphorylation, that reduction is not statistically significant.

Considering that $BRAF^{V600E}$ is important in cell growth, we decide to determine whether or not the 11 selected compounds reduce cell viability as result of BRAF inhibition by using MTT assay. In order to determine the adequate experimental conditions, first we tested cell

Table 1
Structural features of compounds obtained from the virtual screening and evaluated as BRAF inhibitors.

1	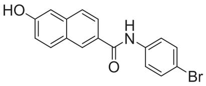	**2**	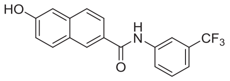
3	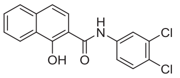	**4**	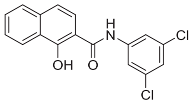
5	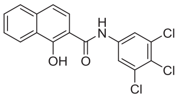	**6**	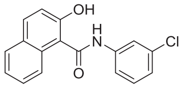
7	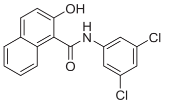	**8**	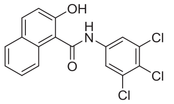
9	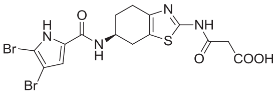	**10**	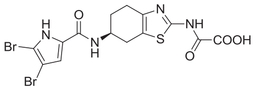
11	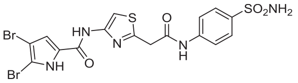	**12**	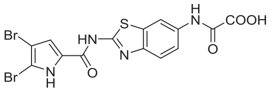
13	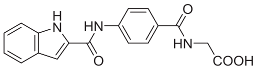	**14**	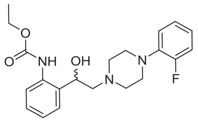
15	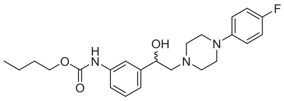	**16**	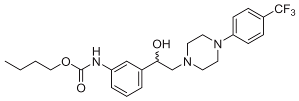
17	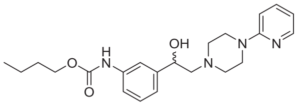	**18**	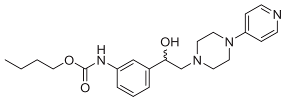
19	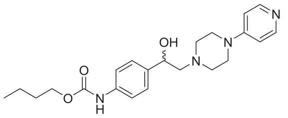	**20**	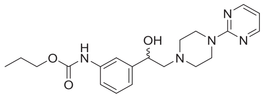
21	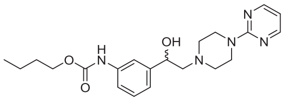	**22**	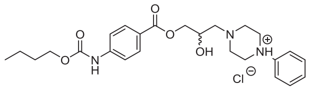
23	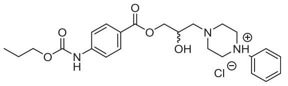		

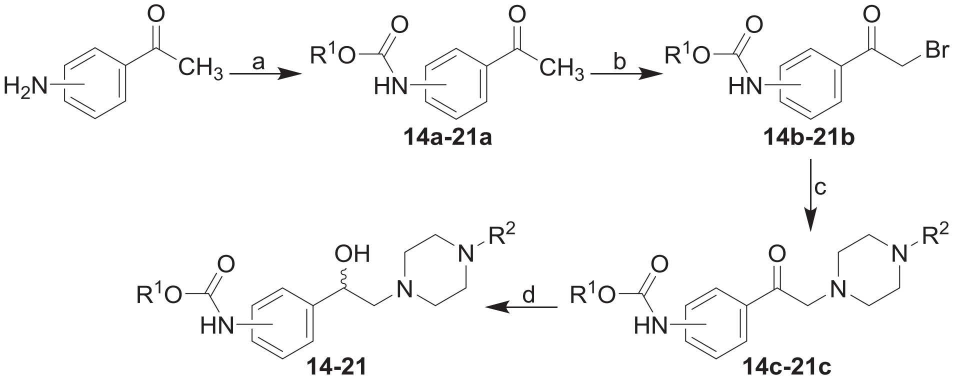

Scheme 1. Synthesis of alkyl {2-/3-/4-[1-hydroxy-2-(4-arylpiperazin-1-yl)ethyl] phenyl}carbamates **3–6**. R^1: 2-Et, 3-Pr, 3-Bu, 4-Bu; R^2: 2-fluorophenyl, 4-fluorophenyl, 4-(trifluoromethyl)phenyl, pyridine-2-yl, pyridine-4-yl, pyrimidine-2-yl. *Reagents and conditions:* (a) $ClCOOR^1$, pyridine, acetone, reflux 3 h; (b) Br_2, $CHCl_3$, ambient temperature 3 hor $CuBr_2$, $CHCl_3$/EtAc, reflux 8 h; (c) *N*-(hetero)arylpiperazine, TEA, THF, ambient temperature 3 h; (d) $NaBH_4$, MeOH, reflux 3 h.

viability of Lu1205 cells treated with Vemurafenib 1 and 10 µM at 48 and 72 h. As shown in Fig. 8A, Lu1205 cells treated with Vemurafenib proliferate less in comparison to the control both at 48 and 72 h. Furthermore, ICW was performed to corroborate that BRAF remains inhibited at 48–72 h of Vemurafenib treatment (Fig. 8B). Since the results were similar at both 48 and 72 h, we decided to use only 72 h for the following experiments.

Subsequently, Lu1205 cells were treated with the 11 selected

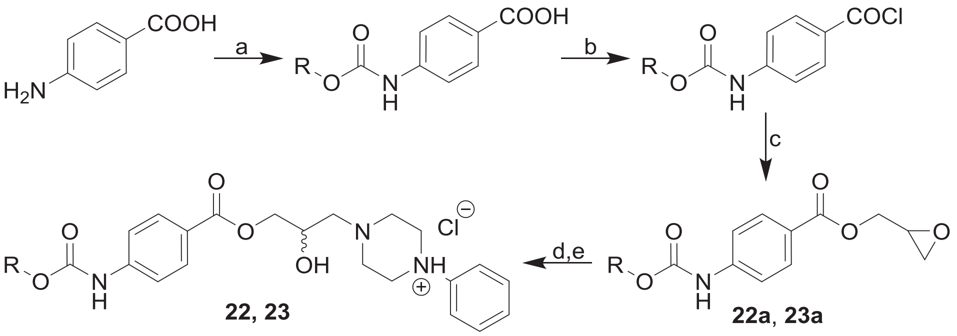

Scheme 2. Synthesis of studied 1-(3-{4-[(alkoxycarbonyl)amino]benzoyloxy}-2-hydroxypropyl)-4-phenylpiperazin-1-ium chlorides **22** and **23**. R: Bu and Pr. *Reagents and conditions*: (a) ClCOOR, pyridine, acetone, reflux 3 h; (b) $SOCl_2$, toluene, reflux; (c) 2,3-epoxypropan-1-ol, THF, TEA, 0 °C then ambient temperature; (d) 1-(4-phenyl)piperazine, *i*-PrOH, reflux; (e) HCl, Et_2O, ambient temperature.

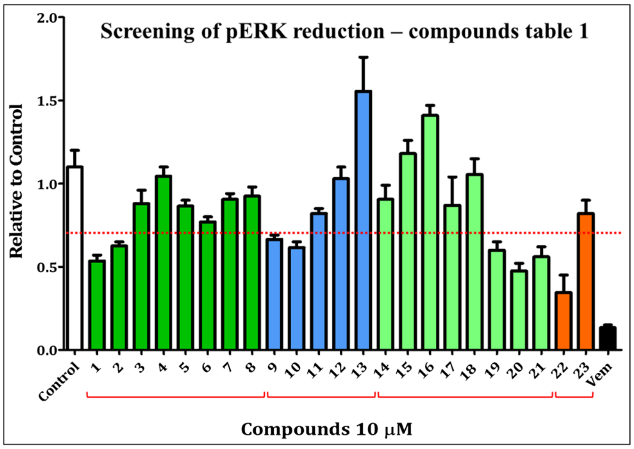

Fig. 6. Results obtained from the initial screening for compounds of Table 1. Substituted hydroxynaphthalenecarboxamides (dark green), N-(hetero)aryl-piperazinylhydroxyalkylphenylcarbamates (blue), substituted piperazinylethanols (light green), and substituted piperazinylpropandiols (orange). The red line indicates the cut between compounds with significant activity of the rest. The graph corresponds to the quantification of pERK of 2 experiments.

compounds at 1 and 10 μM for 72 h. Our results revealed that only compounds **1** and **22** reduced significantly Lu1205 cell viability (Fig. 9).

In summary, we evaluated 23 compounds with different structural scaffolds. From the preliminary study we selected 11 compounds, of which 7 showed significant inhibitory activities. The results of the most exhaustive study show that these 7 compounds reduce ERK phosphorylation. These results indicate the good performance of our screening model. Compounds **1, 9, 20** and **22** have different scaffold and showed the most interesting activities. Among active compounds it is possible to clearly visualize four different types of structural scaffolds: (a) substituted hydroxynaphthalenecarboxamides (compounds **1** and **2**), N-(hetero)aryl-piperazinylhydroxyalkylphenylcarbamates (**9**), substituted piperazinylethanols (**19** and **20**) and substituted piperazinylpropandiols (**22** and **23**). Considering that these compounds have been obtained through a primary screening, their inhibitory activities can be considered quite strong and promising. In this sense, the inhibitory effect obtained for compounds **1** and **22** are very interesting since they showed a strong inhibitory activity even at relatively low concentrations (1 μM). Furthermore, both compounds also reduced significantly cell viability, indicating that the inhibition of ERK signaling is accompanied by an anti-proliferative effect. Although these compounds have a strong inhibitory activity, their effects are weaker than that obtained for Vemurafenib. In the next section we report a molecular modeling study in which we evaluate the molecular interactions of the different L-R (Ligand-Receptor) complexes, which allows us to explain the different activities observed.

2.4. Molecular modeling

In order to understand at molecular level the behavior of these compounds, we conducted a molecular modeling study. The main objective of this study was to evaluate the molecular interactions that stabilize the different molecular complexes. This information could be very useful for the design and modification of these starting structures to obtain compounds with higher affinity for this protein. To this end, we selected a representative compound for each structural scaffold to make a comparative study for compounds **1, 9, 20** and **22**. We also included in our study Vemurafenib, which allowed us to perform a comparative analysis of the different activities displayed by these molecules in relation to their structural differences.

The molecular modeling study was conducted in three different stages. First, we performed a docking analysis using the Autodock program [21]. In the second stage of this study, we carried out molecular dynamics (MD) simulations using the AMBER software package [37]. From the trajectories obtained with MD simulations, we performed an analysis per residue for the different compounds. Finally, to better understand the molecular interactions involved in the different L-R complexes, a Quantum Theory of Atoms In Molecules (QTAIM) study was carried out for the most representative structures. We have previously demonstrated the importance of these QTAIM studies for the understanding of the details of the different molecular interactions that stabilize or destabilize the various complexes [38–45].

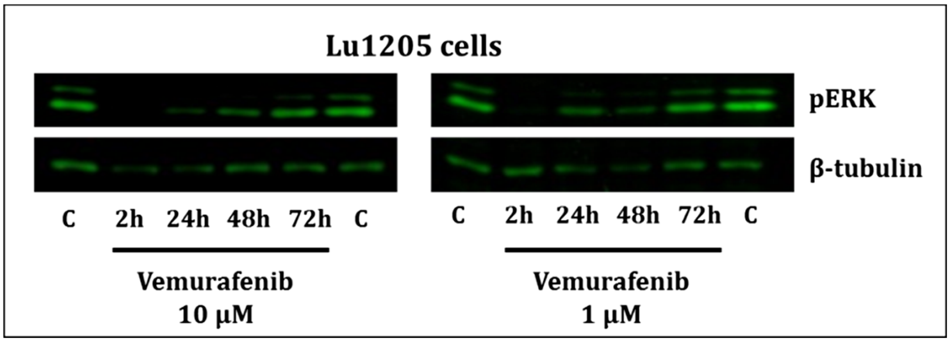

Fig. 5. Lu1205 melanoma cells were treated with 1 and 10 μM of Vemurafenib or Control (untreated cells incubated with the carrier DMSO) at the indicated times. Proteins from cell lysates were separated by SDS-PAGE and transferred onto a nitrocellulose membrane. Membranes were incubated with the primary antibodies as indicated. The image is representative from at least 5 independent experiments.

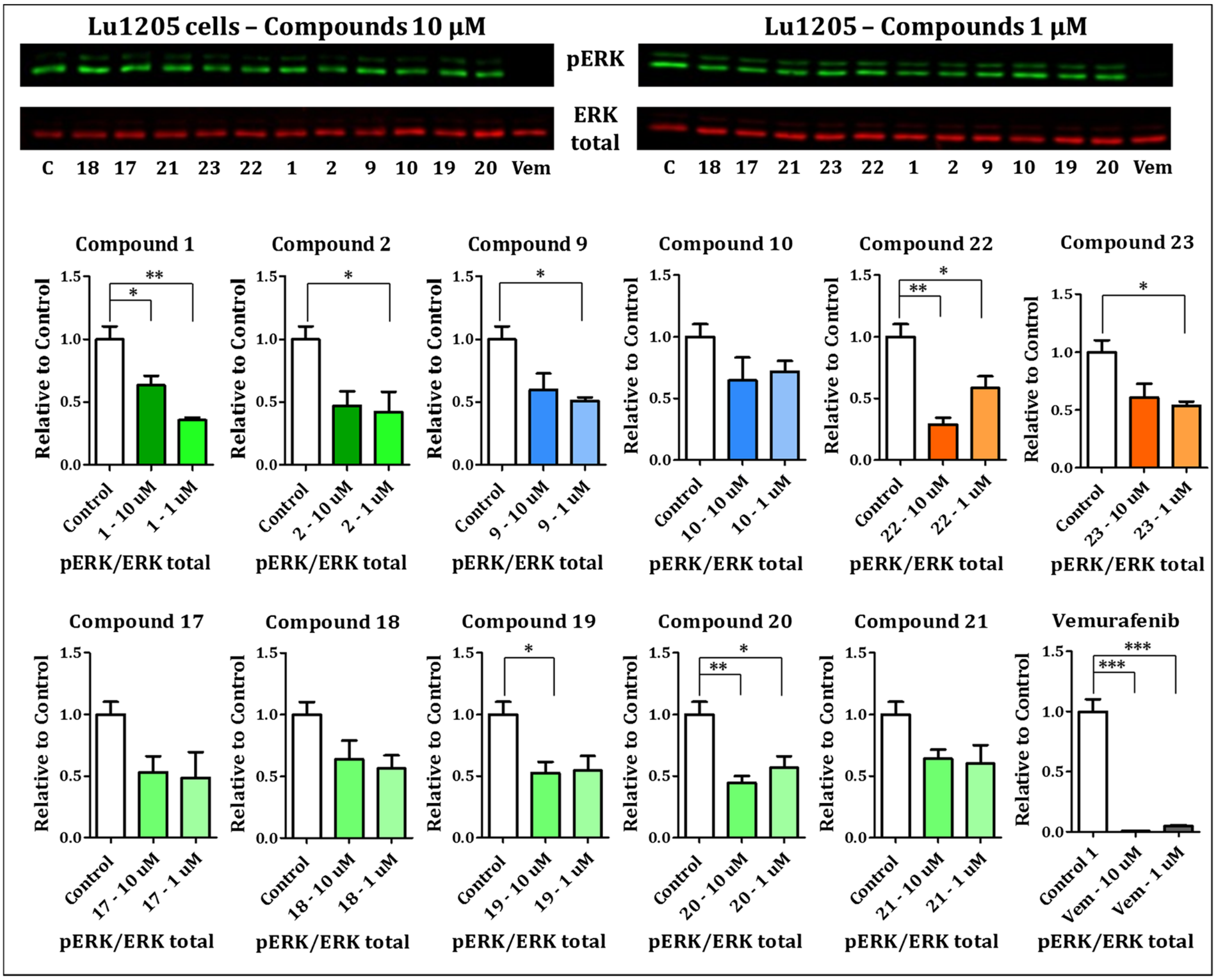

Fig. 7. Lu1205 melanoma cells were treated with the indicated compounds for 2 h at 1 and 10 μM. Proteins from cell lysates were separated by SDS-PAGE and transferred onto a nitrocellulose membrane. Membranes were incubated with the primary antibodies as indicated. The software Image Studio 5.2 was employed for the quantifications. Optical density of pERK band for each treatment was normalized to the respective ERK total band. pERK/ERK total relation for each treatment was relativized to pERK/ERK total relation of the control corresponding to untreated cells incubated with the carrier DMSO. Quantifications correspond to 3 independent experiments and the blots are representative from them. Statistic: One-way ANOVA and Tukey's post-test; (*p ≤ 0,05; **p = < 0,01; ***p ≤ 0,001).

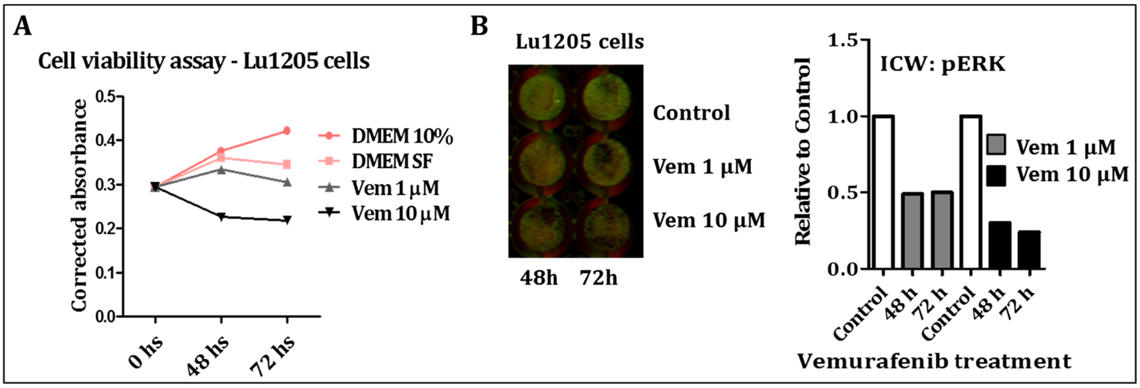

Fig. 8. Lu1205 cells cultured in 96-well plate were treated with Vemurafenib 1 and 10 μM or control. MTT reagent was added at the indicated times and incubated for 3 additional h. Then formazan product was dissolved and absorbance read at 540 nm (A). ICW was performed in parallel to MTT assay (B).

Analysis per residue obtained from molecular dynamics simulations allowed us to define the main interactions that stabilize the different complexes (Fig. 10). Our simulations indicate the importance of the following residues: ILE463, LYS483, LEU505, PHE516, ILE527, TRP531, GLN530, CYS532, PHE583, PHE595 and mainly ASP594 for binding of these ligands to BRAF. These results are in agreement with previously reported experimental data [46].

Superpositions of interactions obtained for compounds **1, 9, 20** and **22** with those displayed by Vemurafenib are shown in Fig. 10a–d. According to this data, it is evident that these compounds bind in a similar manner to Vemurafenib because they interact with essentially the same amino acids. However, these interactions are weaker than those shown for Vemurafenib along the simulations. These results are in agreement with the experimental data and might explain, at least in part, the lower

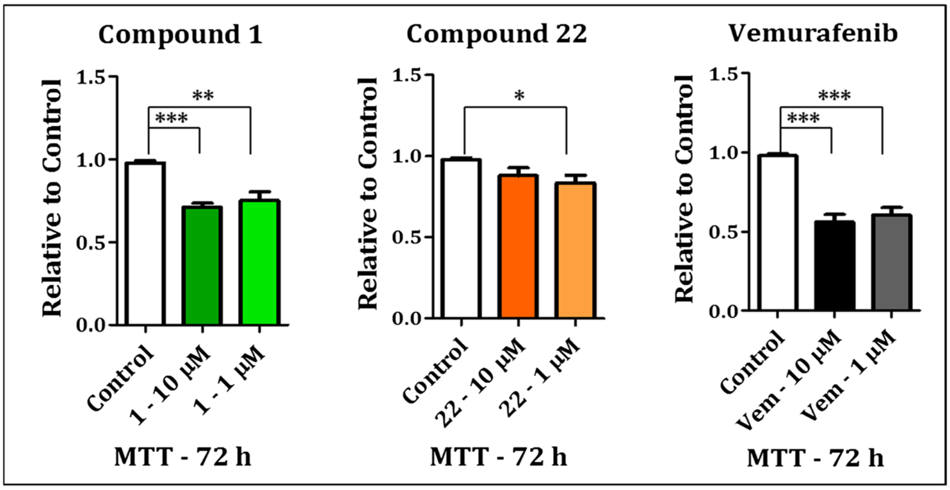

Fig. 9. Lu1205 cells cultured in 96-well plate were treated with the 11 compounds selected previously, Vemurafenib or control (DMSO), at 10 and 1 µM. After 72 h of treatment, MTT reagent was added and incubated for 3 additional h. Then formazan product was dissolved and absorbance read at 540 nm. Each condition was assayed by 6 replicates and the results correspond to 3 independent experiments. One-way ANOVA and Tukey's post-test were performed.

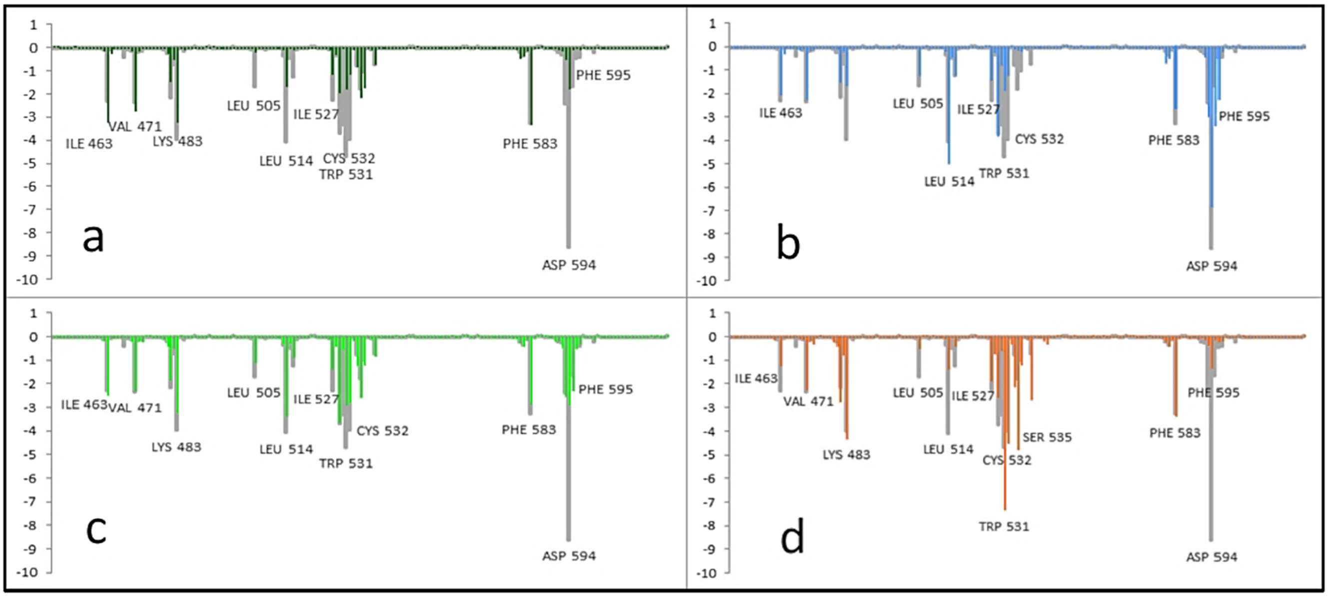

Fig. 10. Over imposed histograms showing the interaction energies of compounds **1** (dark green, a), **9** (light-blue, b), **20** (light-green, c) and **22** (orange, d) with the main amino acids involved in the complex formation. The histogram obtained for Vemurafenib is shown in gray in all the histograms for comparison.

inhibitory effects of the compounds reported here than Vemurafenib. Active compounds displayed their pharmacophoric portions in a closely related spatial form to that displayed by Vemurafenib [46]. This might be well appreciated in Fig. 11.

The main objective of our molecular modeling study is to evaluate the molecular interactions that stabilize the different ligand-enzyme complexes. It is well known that simulations of molecular dynamics are too crude, and that they might miss important information and many details involved in the stability of molecular complexes. Thus, we decided to conduct a QTAIM study that can better quantify the molecular interactions obtained for the different complexes. In fact, our research's group has been the pioneer in this type of studies and in many of them we have demonstrated the ability of QTAIM calculations to evaluate the molecular interactions for this type of complexes [38–45].

Fig. 12 shows the charge density sum at intermolecular bond critical points (BCPs). Inhibitors contributions to anchoring at the DFG-loop and hinge regions of ATP binding site are stacked on top of each other. As depicted in this figure, Vemurafenib is more strongly anchored to the enzyme ATP binding site than inhibitors reported here, as evidenced by the total height of stacked bars. Moreover, separate contributions to anchoring at the Hinge and DFG-loop regions of ATP binding cleft tell us which interactions need to be optimized in order to increase binding affinity of the new inhibitors.

On the other hand, when comparing $\Sigma\rho$ values and inhibitory activities of moderate inhibitors as the ones reported here, no evident relationship is found. It should note that the four compounds reported here displayed similar inhibitory effect; however compounds **1** and **20** are more weakly anchored to the enzyme binding cleft according to the $\Sigma\rho$ values.

Separate contributions to anchoring at the Hinge and DFG-loop regions of ATP binding cleft (see Fig. 12) show that Vemurafenib as well as the two most active inhibitors reported here (**1** and **22**) show a stronger anchoring at the hinge region as compared to compounds **9** and **20**. Moreover, these inhibitors also have in common that anchoring at both DFG-loop and hinge has similar strength, namely they show a balanced anchoring at both ATP binding cleft regions.

Comparing ATP binding mode with those found for Vemurafenib and the new inhibitors from Molecular Dynamic simulations (Fig. 11) it is easy to identify which part of the inhibitors mimic the interactions of adenine and which other parts mimic the triphosphate (and less clearly ribose) interactions. Adenine moiety from ATP binds to the hinge

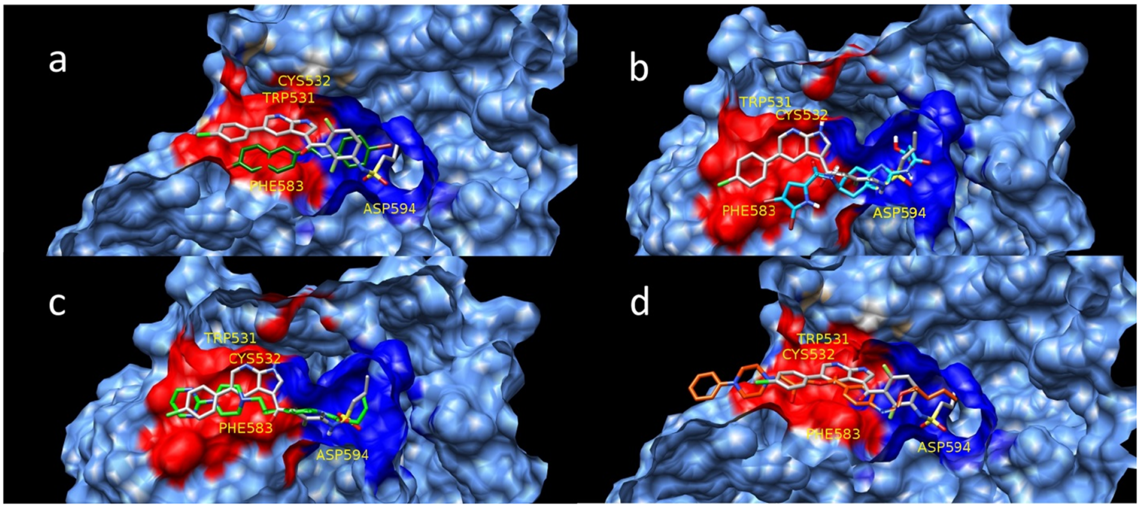

Fig. 11. View of the spatial ordering adopted by the different ligands in the active site of BRAF. Compounds **1** (dark green), **9** (light-blue), **20** (light-green) and **22** (orange) are over imposed with Vemurafenib in gray color. All these compounds are docked to a similar conformation of BRAF.

region of the binding cleft while triphosphate group binds to the DFG-loop. Therefore, the hinge and DFG-loop interacting parts of inhibitors are depicted in red and blue respectively, in the subsequent charge density molecular graphs.

The charge density molecular graphs in Fig. 13 displayed the main interactions of Vemurafenib at ATP binding site of BRAF kinase. For easy viewing, interactions of arylsulfonamide moiety that substitutes position 3 of the azaindole ring are shown in Fig. 13A whereas interactions of azaindole as well as its substituent at position 5 are depicted in Fig. 13B.

The sulfonamide moiety of Vemurafenib resembles ATP phosphate groups. In that way, it forms strong interactions with the DFG motif of the activation segment as long as it is in the “in” conformation. As shown in Fig. 13A, the sulfonamide oxygen atoms are connected through bond paths to the backbone of ASP594 while the amide proton is interacting with ASP594 side chain oxygen. The propyl tail of Vemurafenib is anchored in a hydrophobic pocket where it interacts with side chains of residues PHE595, ILE527, PHE516 and LEU505. The formation of this hydrophobic pocket is a consequence of the disruption of the conserved salt bridge between GLU501 and LYS483 that holds together the αC-helix and the β3-sheet. The propyl tail of Vemurafenib pushes out the αC-helix which in turn causes the salt bridge breaking and the formation of the hydrophobic pocket between αC-helix and β3-sheet. The hydrophobic pocket is shown in surface representation in Fig. 13A. Moreover, LYS483 is stacked over the phenyl ring of the arylsulfonamide moiety and there are several bond paths connecting both groups. Moreover, PHE498 is also helps hold in place the phenyl ring as well as the sulfonamide moiety of Vemurafenib. This residue hangs over the binding cleft and usually do not interact directly with inhibitor because the conserved salt bridge blocks its access to the binding cleft. Thus, interactions of PHE498 are a feature specific to this type of DFG-in αC-helix-out BRAF conformation where the salt bridge is broken.

In that regard, the heterocyclic or azaindole ring of Vemurafenib mimics the interactions of ATP adenine ring and, as it was described in Fig. 13B, heterocyclic ring lies in the plane of the hinge loop and forms several interactions with backbone atoms of this loop. The pyridine nitrogen atom acts as hydrogen bond acceptor against the backbone amide hydrogen of CYS532 whereas the proton attached to pyrrole nitrogen acts as hydrogen bond donor against the carbonyl oxygen of GLN530. Other residues above and below the plane of the hinge loop also help to keep the heterocyclic ring in place by forming interaction with the π electrons of this ring. Above the plane of the hinge loop, side

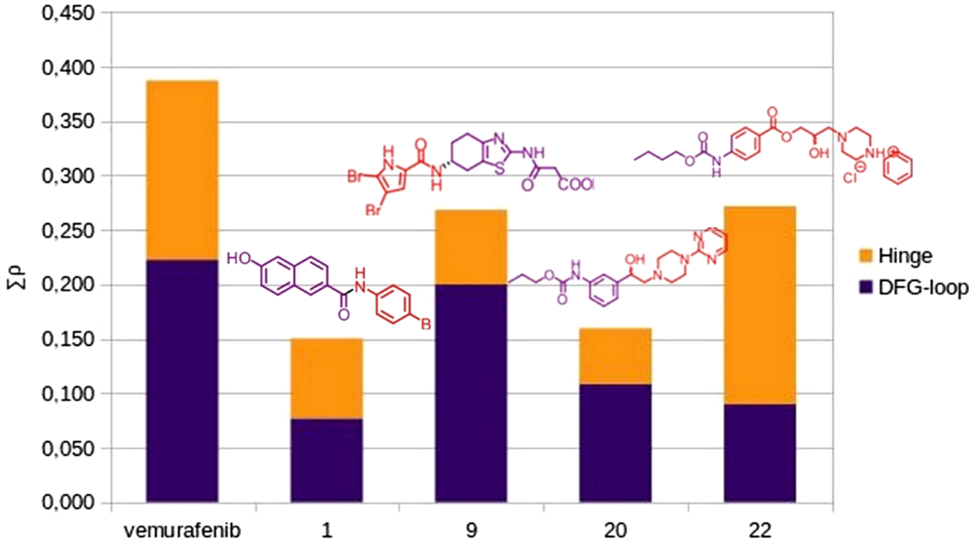

Fig. 12. Charge density sum at the intermolecular BCPs for complexes of BRAF with selected inhibitors. The interactions corresponding to the adenine-like moiety of inhibitors has been colored in orange, whereas the interactions of the inhibitors that resemble the ATP triphosphate interactions are depicted in magenta.

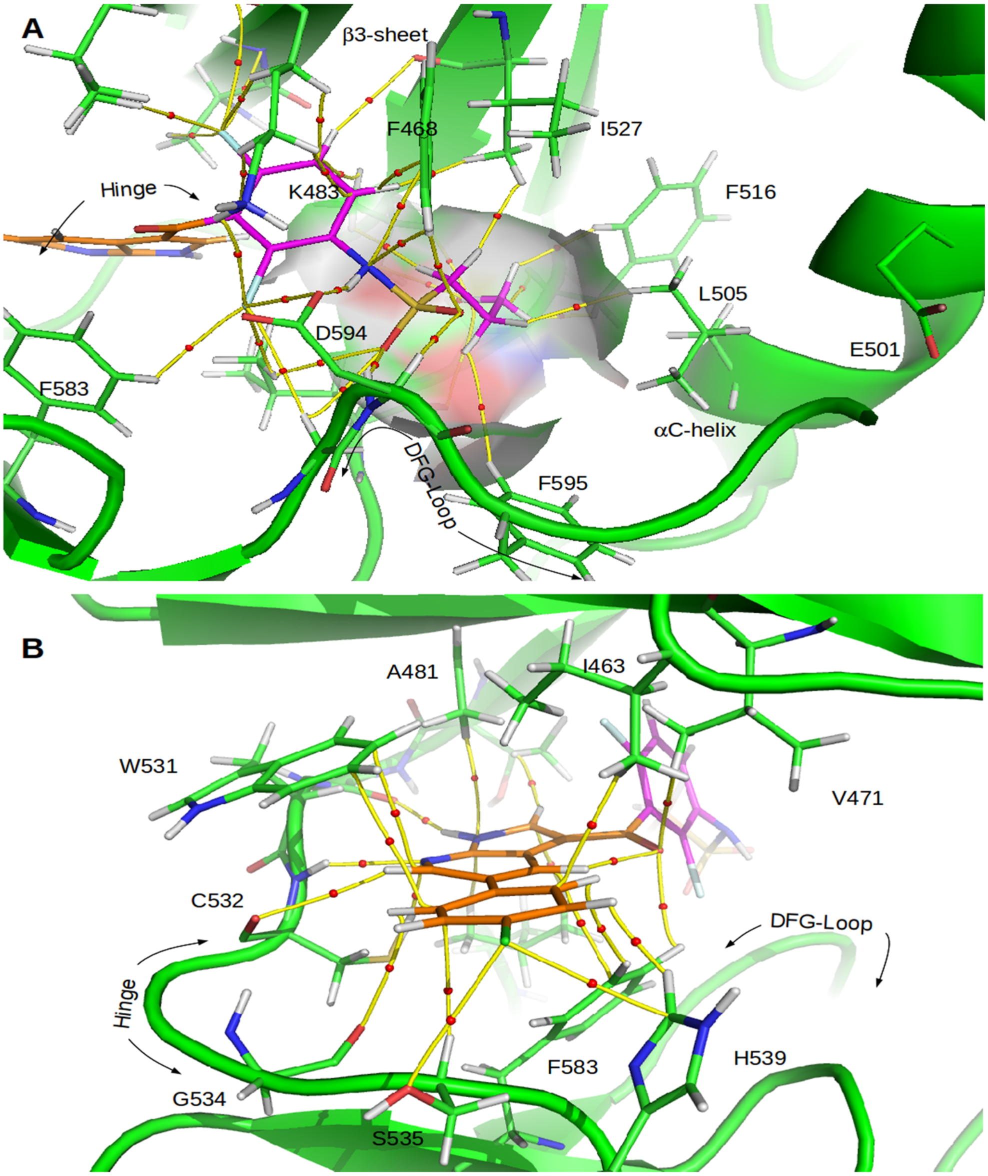

Fig. 13. Charge density molecular graphs depicting the molecular interactions of Vemurafenib at the ATP binding site. Yellow lines connecting the nuclei are the Bond Paths (BPs) and small red circles over them are the Bond Critical Points (BCPs). For easy viewing, interactions with DFG-loop and Hinge region are depicted separately in panels A and B, respectively. The interacting portions of DFG-loop and Hinge of Vemurafenib are colored in purple and orange, respectively.

chain of residues ILE463 and ALA481 act as hydrogen bond donor against the π system of the heterocyclic ring while side chain of TRP531 forms face to face stacking interactions with that ring. Below the plane of the hinge loop, PHE583 forms stacking interaction with azaindole ring and sulfhydryl proton from CYS532 acts as hydrogen bond donor against the pyridine nitrogen. The chlorophenyl ring attached to the azaindole also forms stacking interactions with PHE582 and TRP531.

Figs. 14–17 show the charge density molecular graphs of inhibitors reported in this work as they bind in the BRAF binding cleft.

As can be seen in Fig. 14, carboxylic acid oxygen atom of compound **9** forms strong interactions with backbone of DFG-loop that resemble interactions of sulfonamide oxygen atom of Vemurafenib with the same loop. In fact, DFG-loop interacting part of compound **9** is anchored with almost the same strength to the ATP binding cleft as Vemurafenib (Fig. 12). On the other hand, hinge interacting part of compound **9** fails in adopting the ATP adenine-like binding mode in which heterocycle lies in the same plane as the hinge backbone loop. Instead, the compound **9** brominated pyrrole ring is anchored above that plane with an interaction pattern similar to Vemurafenib but much weaker. It forms stacking interactions with side chains of residues TRP531 and ILE463 above and PHE583 below the hinge plane, resembling interactions of Vemurafenib with the same residues. However, some of the strong interactions formed by Vemurafenib with the backbone of the hinge are either missed or very weak. It is evident that anchoring of compound **9** is driven by the DFG-loop interacting part of the inhibitor which might explain the deficient binding of the hinge interacting portion.

In a similar fashion, compound **20** (Fig. 15) also shows a deficient binding to enzyme hinge loop that can be explained in the same way as in compound **9** complex, namely it is the DFG-loop interacting part which governs the overall binding mode of the inhibitor (Fig. 12). In addition to interactions with backbone of DFG-loop, compound **20** is anchored in the hydrophobic pocket between αC-helix and β3-sheet through its terminal *n*-butyl chain that resemble Vemurafenib *n*-propyl chain. Hydrophobic interactions formed by *n*-butyl chain are represented in the molecular graph of Fig. 15 by bond paths connecting hydrogen atoms of that chain with the same atoms of residues VAL501, LEU505, PHE516, ILE527 and PHE595. These hydrophobic interactions together make a non-negligible contribution to anchoring.

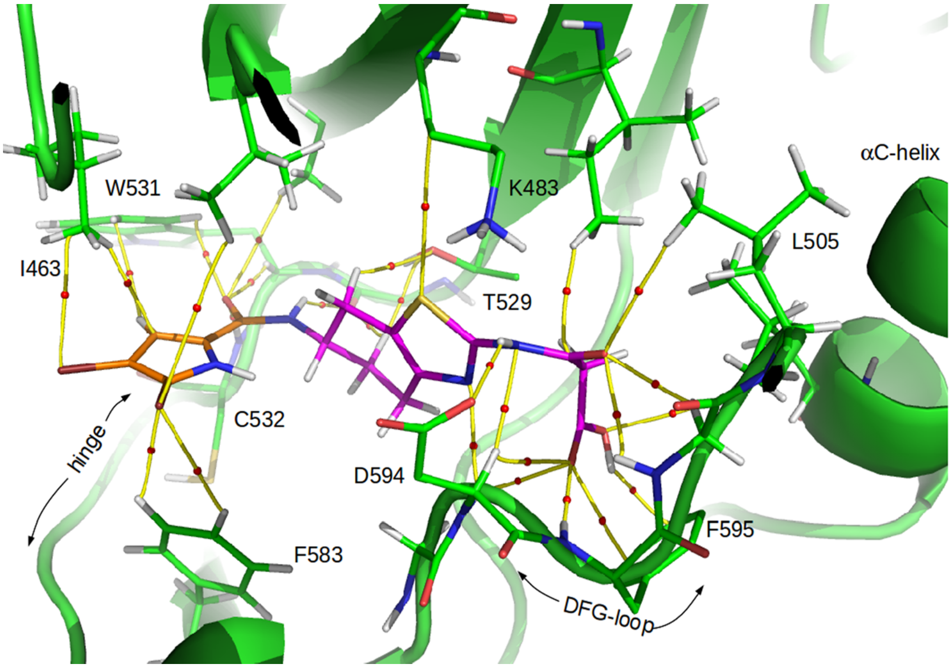

Fig. 14. Compound **9** interactions at the BRAF binding cleft. Topological elements of the charge density for the intermolecular interactions are depicted: bond paths in yellow lines and BCPs in red circles. The atoms of the inhibitor interacting with DFG-loop and hinge regions are colored in purple and orange, respectively.

Unlike to compounds **9** and **20**, the remaining inhibitors reported in this work, compounds **1** and **22** are either more strongly anchored to the hinge loop as in the case of **22** or show a balanced anchoring at both ATP binding cleft regions as in the case of **1**.

As evidenced in Fig. 16, hinge interacting ring of compound **1** lies close to the plane of the hinge region forming interactions with residues ILE463 and PHE583 above and below the plane, respectively. Additionally, hydroxyl group atacched to β-naphtyl moiety of compound **1** is connected through several bond paths to the side chain of residues SER535 and SER536 from the hinge loop and also to HIS539. However, compound **1** lacks interactions with backbone of the hinge characteristic of ATP adenine ring which explains its modest binding to that loop as compared to Vemurafenib. On the other side, bromophenyl moiety from DFG interacting part of compound **1** is anchored to the ATP binding cleft almost exclusively through hydrophobic interactions involving the bromine atom. This rather weak anchoring of DFG interacting part would allow a better positioning (and slighly stronger binding) of the hinge interacting part of compound **1** as compared to **9** and **20**. The modest improvement in hinge interacting part anchoring seems to be related to increased inhibition of the first compound with respect to the last ones.

Similarly than compound **1**, DFG-loop interacting part of compound

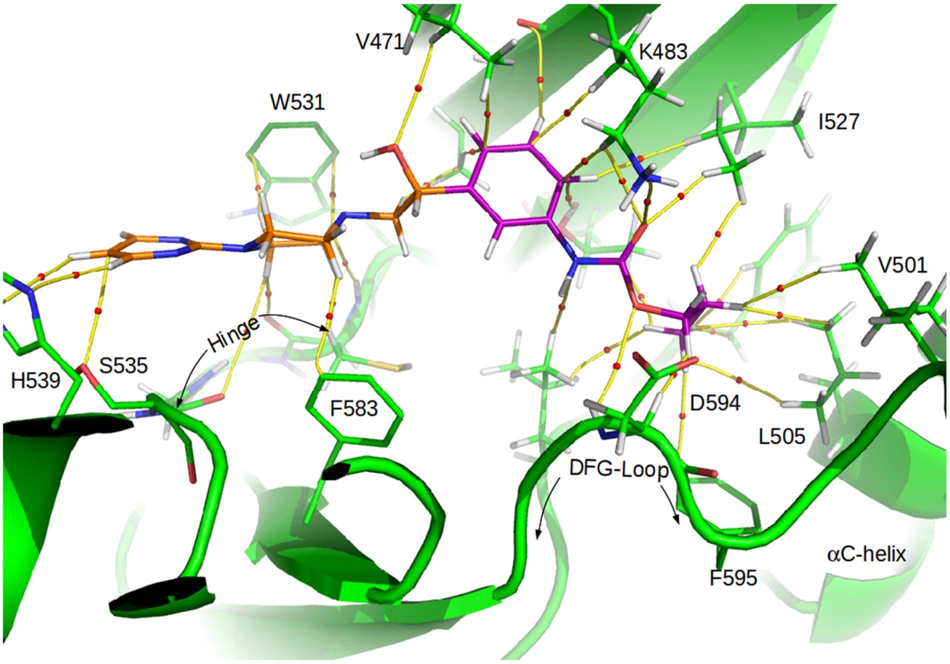

Fig. 15. Interactions of compound **20** at the BRAF binding cleft. Topological elements of the charge density for the intermolecular interactions are depicted: bond paths in yellow lines and BCPs in red circles. Inhibitor atoms interacting with DFG-loop and hinge regions colored in purple and orange, respectively.

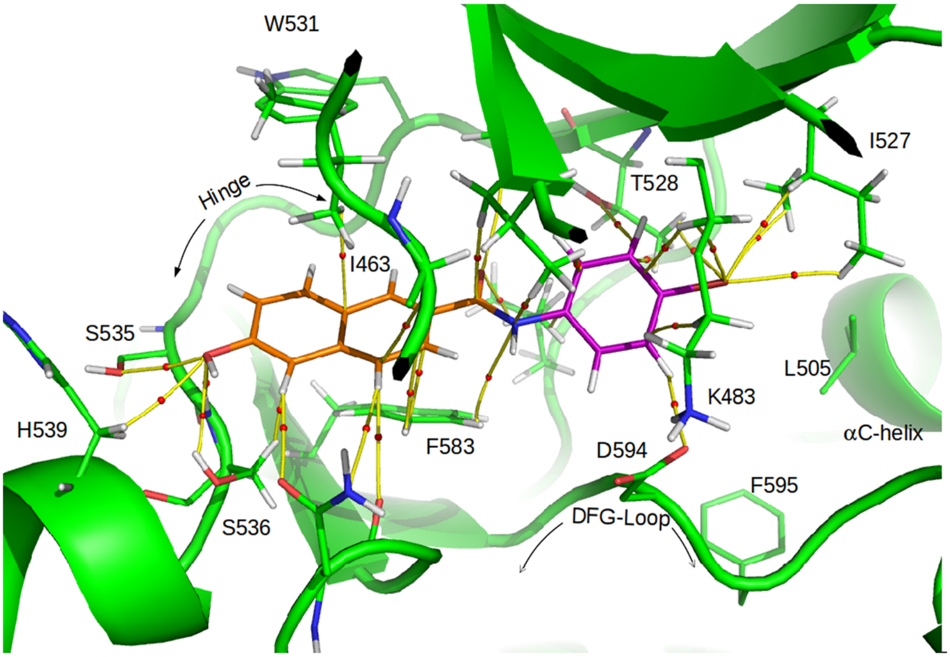

Fig. 16. Interactions of compound **1** at the BRAF binding cleft. Topological elements of the charge density for the intermolecular interactions are depicted: bond paths in yellow lines and BCPs in red circles. Inhibitor atoms interacting with DFG-loop and hinge regions colored in purple and orange, respectively.

22 (Fig. 17) binds to the ATP binding cleft mostly through weak nonpolar interactions involving its *n*-butyl terminal chain. As shown in Fig. 12, anchoring of that portion of compound **22** is rather weak as compared with the binding strength of the hinge interacting part. Thus, the anchoring of compound **22** is driven by the interaction with the hinge region of the enzyme. Again, binding strength at the hinge region seems to correlate better with the inhibition activity than full inhibitor anchoring strength, since compound **22** is more active than **9** even when the total anchoring strength is almost the same for both inhibitors. Note that the only difference is that compound **22** is more strongly anchored to the hinge region while anchoring of **9** is driven by the DFG-loop interacting part, as discussed earlier.

3. Conclusions

The oncogenic kinase BRAF is mutated in many types of cancer, including melanoma, thyroid cancer, leukemia, colon cancer, among others. Particularly in melanoma, around 50% of patients harbor the mutated kinase BRAF^{V600E} that promotes cancer progression and development [1]. Melanoma is the deadliest form of skin cancer and according to the registers of the International Agency for Research in Cancer (IARC) its incidence has been growing in the last 20 years around the world (http://gco.iarc.fr/). Vemurafenib and Dabrafenib are two specific BRAF inhibitors that are approved for melanoma treatment. However resistance to anti BRAF therapy and secondary side effects limits its usefulness, making necessary the search of new inhibitors that could overcome these drawbacks.

Our theoretical and experimental study has allowed us to find four new structural scaffolds (eleven compounds), which could be used as excellent starting structures for the design and development of new inhibitors of BRAF. Such study was carried out in four steps: virtual screening, synthesis, bioassays and molecular modeling and has allowed us to propose compounds **1, 9, 20** and **22** as excellent starting structures for the development of new BRAF inhibitors. It should be noted that these compounds have been obtained from a primary screening and therefore their inhibitory activities can be considered as very significant and promising. In this sense hydroxynaphthalenecarboxamides, N-(hetero)aryl-piperazinylhydroxyalkylphenylcarbamates, piperazinylethanols and piperazinylpropandiols motifs represent novel cores for BRAF inhibitors and might find application to the design and development of new inhibitors.

Another interesting contribution of this work is the insight into details of certain structural aspects which are essential for understanding the formation of the complex ligand-BRAF interactions. Our QTAIM study has provided details on the molecular interactions that stabilize the formation of complexes of Vemurafenib with BRAF. Regarding the results obtained for the complexes of **1, 9, 20** and **22** with BRAF, such data give us an excellent guide to know which portions of these molecules should be modified in order to improve their affinity for the enzyme. It is important to remark that such information cannot be obtained using a simple method like the docking techniques or even only by using MD simulations. To obtain more detailed information about these molecular complexes, it is necessary to use more specific techniques, like for example QTAIM calculations. In fact the use of combined techniques: docking, MD simulations and QTAIM calculations, give us information about two important aspects: (i) why these novel compounds are less potent BRAF inhibitors than Vemurafenib, and (ii) crucial information about what portion of these compounds should be modified in order to increase their affinity for BRAF.

In summary, our findings provide useful information about novel structural scaffolds that reduce ERK phosphorylation and viability in BRAF^{V600E} melanoma cells. We expect that these scaffolds will serve as a start point to obtain better and more specific BRAF^{V600E} inhibitors that may potentially diminish resistance occurrence and improve the response and durability of current therapies against BRAF^{V600E}-harboring cancers.

4. Experimental section

4.1. Synthesis of N-(substituted phenyl)-hydroxynaphthalene-carboxamides 1–8

Described anilides **1**, **2** were characterized by Kos et al. [24], anilides **2–5** and **7** were characterized recently by Gonec et al. [25] and anilide **6** was characterized by Gonec et al. [26].

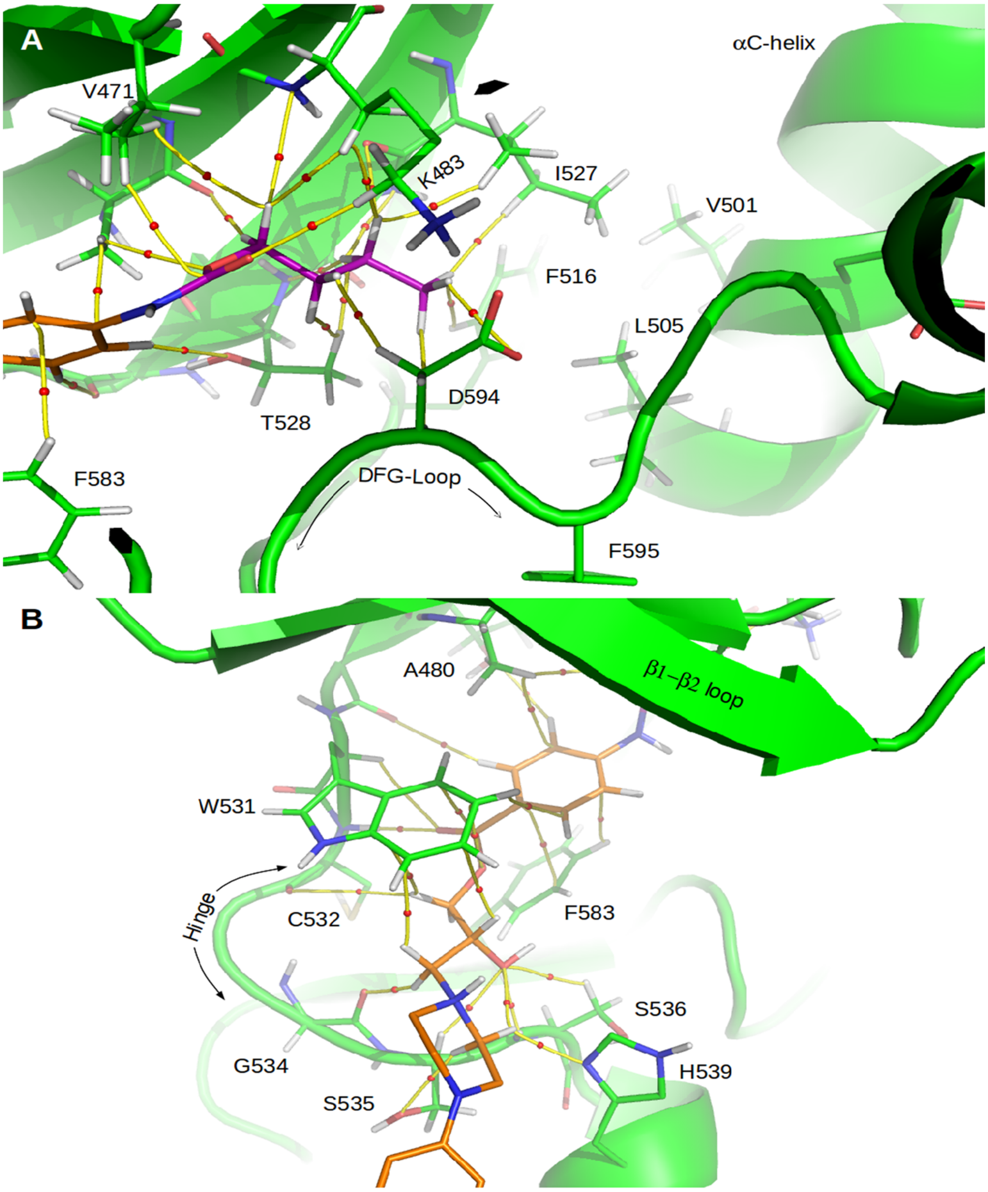

Fig. 17. Charge density molecular graphs depicting the molecular interactions of compound **22** at the ATP binding site. For easy viewing, interactions with DFG-loop and Hinge region are depicted separately in panels A and B, respectively.

4.2. Synthesis and characterization of compounds 9–13

Synthesis and characterization of compounds **9–13** have been previously reported [27–30] (See Supplementary Information).

4.3. Synthesis of compounds 14–21 (Scheme 1)

General information

Commercially available compounds were used as received, unless stated otherwise. Melting points were measured by a Kofler hot plate apparatus HMK (Franz KustnerNacht GK, Dresden, Germany) and are uncorrected. TLC was performed on silica gel 60 F_{254} on aluminium plates (Merck, Darmstadt, Germany) and visualized with UV light (254 nm). Residues were purified by silica gel 60 (40–63 µm, Merck 9385) column chromatography. Infrared (IR) spectra were recorded on a Smart MIRacle™ ATR ZnSe for Nicolet™ Impact 410 Fourier-transform IR spectrometer (Thermo Scientific, West Palm Beach, FL, USA). The spectra were obtained by the accumulation of 256 scans with 2 cm^{-1} resolution in the region of 4000–650 cm^{-1}. ^{1}H NMR and ^{13}C NMR spectra were standardly recorded at 25 °C in DMSO-d_6 as solvents on an Avance III 400 MHz FT-NMR spectrometers (Bruker, Karlsruhe, Germany). ^{1}H and ^{13}C chemical shifts (δ) are reported in ppm. High-resolution mass spectra (HRMS) were measured using a high-performance liquid chromatograph DionexUltiMate® 3000 (Thermo Scientific, West Palm Beach, FL, USA) coupled with a LTQ Orbitrap XL™ Hybrid Ion Trap-Orbitrap Fourier Transform Mass Spectrometer (Thermo Scientific) with injection into HESI II in the positive or negative mode.

Butyl (3-acetylphenyl)carbamate(**15a–18a** = **21a**), butyl (4-acetylphenyl)carbamate(**19a**), butyl [3-(bromoacetyl)phenyl]carbamate (**15b–18b** = **21b**), butyl [4-(bromoacetyl)phenyl]carbamate (**19b**), butyl {3-[(4-(pyridine-4-yl)piperazin-1-yl)acetyl]phenyl}carbamate (**18c**), butyl {4-[(4-(pyridine-4-yl)piperazin-1-yl)acetyl]phenyl}carbamate (**19c**) and final butyl {3-[1-hydroxy-2-(4-(pyridine-4-yl)piperazin-1-yl)ethyl]phenyl}carbamate (**18**), butyl {4-[1-hydroxy-2-(4-(pyridine-4-yl)piperazin-1-yl)ethyl]phenyl}carbamate (**19**) were previously reported [44].

*4.3.1. General procedure for the preparation of alkyl (2-/3-acetylphenyl) carbamates (**14a–21a**)*

A solution of an appropriate alkyl chloroformiate (37 mmol) in acetone (5 mL) was added dropwise to a stirred solution of 2-aminoacetophenone (5.00 g; 37 mmol) or 3-aminoacetophenone (5.00 g; 37 mmol) and pyridine (3.0 mL; 37 mmol) in acetone (20 mL), and then the mixture was heated to reflux for 3 h. The solvent was removed at reduced pressure, and the resulting solid was washed with water, and recrystallized from EtOH.

*4.3.1.1. Ethyl (2-acetylphenyl)carbamate (**14a**).* White solid, Yield 97%, m.p. 87–90 °C [90 °C [47,48]. ^{1}H NMR (DMSO-d_6) δ 1.24 (t, 3H, $-$CH$_3$, $J = 7.3$ Hz), 2.63 (s, 3H, COCH$_3$), 4.10 (q, 2H, OCH$_2-$, $J = 7.3$ Hz), 7.15 (t, 1H, ArH, $J = 7.7$ Hz), 7.61 (t, 1H, ArH, $J = 7.9$ Hz), 8.03 (d, 1H, ArH, $J = 7.7$ Hz), 8.24 (d, 1H, ArH, $J = 8.4$ Hz), 10.99 (s, 1H, NH) [49]. ^{13}C NMR (DMSO-d_6) δ 202.73, 152.93, 139.81, 134.42, 132.00, 122.28, 121.75, 118.52, 60.68, 28.44, 14.78.

*4.3.1.2. Propyl (3-acetylphenyl)carbamate (**20a**).* White solid, Yield 83%, m.p. 101–103 °C.^{1}H NMR (DMSO-d_6) δ 0.94 (t, 3H, $-$CH$_3$; $J = 7.5$ Hz), 1.59–1.69 (m, 2H, $-$CH$_2-$), 2.53 (s, 3H, COCH$_3$), 4.06 (t, 2H, OCH$_2-$, $J = 6.6$ Hz), 7.44 (t, 1H, ArH, $J = 7.9$ Hz), 7.61 (d, 1H, ArH, $J = 8.1$ Hz), 7.70 (d, 1H, ArH, $J = 8.1$ Hz), 8.09 (s, 1H, ArH), 9.85 (s, 1H, NH). ^{13}C NMR (DMSO-d_6) δ 197.45, 153.59, 139.60, 137.36, 128.96, 122.57, 122.27, 117.28, 65.73, 26.51, 21.76, 10.06.

*4.3.2. General procedure for the preparation of alkyl [2-/3-(bromoacetyl) phenyl]carbamates (**14b–21b**)*

Powdered CuBr$_2$ (80 mmol) was suspended in dry ethyl acetate (40 mL) and heated. Into a stirred refluxing suspension, a solution of appropriate alkyl (2-/3-acetylphenyl)carbamate (40 mmol) in chloroform (40 mL), was added dropwise and the mixture was refluxed for 8 h. Transformation of black CuBr$_2$ to white CuBr indicated completion of the reaction. Precipitate of CuBr was filtered off and the solvents were removed under reduced pressure. Solid crude products were recrystallized from *i*-PrOH.

*4.3.2.1. Ethyl [2-(bromoacetyl)phenyl]carbamate (**14b**).* White solid, Yield 79%, m.p. 102–104 °C [102–104 °C [50]. ^{1}H NMR (DMSO-d_6) δ 1.26 (t, 3H, $-$CH$_3$, $J = 7.3$ Hz), 4.16 (q, 2H, OCH$_2-$, $J = 7.3$ Hz), 4.95 (s, 2H, CH$_2$Br), 7.19 (t, 1H, ArH, $J = 7.7$ Hz), 7.65 (t, 1H, ArH, $J = 7.9$ Hz), 8.01 (d, 1H, ArH, $J = 8.1$ Hz), 8.15 (d, 1H, ArH, $J = 8.4$ Hz), 10.55 (s, 1H, NH). ^{13}C NMR (DMSO-d_6) δ 195.19, 153.03, 139.82, 134.76, 131.42, 122.09, 121.04, 119.42, 60.86, 35.01, 14.16.

*4.3.2.2. Propyl [3-(bromoacetyl)phenyl]carbamate (**20b**).* White solid, Yield 89%, m.p. 107–110 °C.^{1}H NMR (DMSO-d_6) δ 0.93 (t, 3H, $-$CH$_3$; $J = 7.3$ Hz), 1.59–1.69 (m, 2H, $-$CH$_2-$), 4.05 (t, 2H, OCH$_2-$, $J = 6.6$ Hz), 4.88 (s, 2H, CH$_2$Br), 7.46 (t, 1H, ArH, $J = 7.9$ Hz), 7.67–7.74 (m, 2H, ArH), 8.10 (s, 1H, ArH), 9.90 (s, 1H, NH). ^{13}C NMR (DMSO-d_6) δ 191.43, 153.59, 139.81, 134.51, 129.17, 123.30, 122.93, 117.61, 65.81, 33.70, 21.76, 10.13.

*4.3.3. General procedure for preparation of alkyl {2-/3-[(4-arylpiperazin-1-yl)acetyl]phenyl} carbamates (**14c–21c**)*

A solution of arylpiperazine (5.5 mmol) and triethylamine (0.8 mL; 5.5 mmol) in anhydrous THF (20 mL) was added dropwise to a stirred solution of an appropriate alkyl [2-/3-(bromoacetyl)phenyl]carbamate (5.5 mmol) in anhydrous THF (30 mL), and the mixture stirred for 3 h at ambient temperature. The solvents were removed under reduced pressure, and added chloroform (100 mL) and water. The organic phase was washed with additional water, dried over anhydrous sodium sulfate and the solvent removed under reduced pressure, to give a solid crude product, which was recrystallized from acetone.

*4.3.3.1. Ethyl (2-{[4-(2-fluorophenyl)piperazin-1-yl]acetyl}phenyl) carbamate (**14c**).* Yellow solid, Yield 93%, m.p. 138–142 °C.^{1}H NMR (DMSO-d_6) δ 1.25 (t, 3H, $-$CH$_3$, $J = 7.0$ Hz), 2.66–2.70 (m, 4H, 2,6-piperazine), 2.99–3.06 (m, 4H, 3,5-piperazine), 3.91 (s, 2H, COCH$_2$N), 4.15 (q, 2H, OCH$_2-$, $J = 7.1$ Hz), 6.98–7.17 (m, 5H, ArH), 7.61 (t, 1H, ArH, $J = 7.3$ Hz), 8.09 (d, 1H, ArH, $J = 8.1$ Hz), 8.18 (d, 1H, ArH, $J = 8.4$ Hz), 10.89 (s, 1H, NH). ^{13}C NMR (DMSO-d_6) δ 200.94, 154.87 (d, $J = 242.8$ Hz), 153.09, 139.73 (d, $J = 8.4$ Hz), 139.70, 134.27, 131.10, 124.67 (d, $J = 3.0$ Hz), 122.42, 122.14 (d, $J = 7.6$ Hz), 121.91, 119.17, 119.14 (d, $J = 2.3$ Hz), 115.78 (d, $J = 20.5$ Hz), 64.64, 60.74, 52.47, 49.97 (d, $J = 3.1$ Hz), 14.22.

*4.3.3.2. Butyl (3-{[4-(4-fluorophenyl)piperazin-1-yl]acetyl}phenyl) carbamate (**15c**).* Yellow solid, Yield 88%, m.p. 60–64 °C.^{1}H NMR (DMSO-d_6) δ 0.92 (t, 3H, $-$CH$_3$, $J = 7.3$ Hz), 1.33–1.43 (m, 2H, $-$CH$_2-$), 1.58–1.66 (m, 2H, $-$CH$_2-$), 2.68–2.72 (m, 4H, 2,6-piperazine), 3.08–3.12 (m, 4H, 3,5-piperazine), 3.93 (s, 2H, COCH$_2$N), 4.11 (t, 2H, OCH$_2-$, $J = 6.6$ Hz), 6.93–7.08 (m, 4H, ArH), 7.44 (t, 1H, ArH, $J = 8.1$ Hz), 7.66–7.72 (m, 2H, ArH), 8.14 (s, 1H, ArH), 9.85 (s, 1H, NH). ^{13}C NMR (DMSO-d_6) δ 196.19, 155.94 (d, $J = 235.0$ Hz), 153.57, 147.77 (d, $J = 3.5$ Hz), 139.57, 136.32, 128.90, 122.72, 122.10, 117.31, 117.05 (d, $J = 7.6$ Hz), 115.09 (d, $J = 21.4$ Hz), 63.37, 52.47, 48.73, 30.44, 18.46, 13.42.

*4.3.3.3. Butyl [3-({4-[4-(trifluoromethyl)phenyl]piperazin-1-yl}acetyl) phenyl]carbamate (**16c**).* White solid, Yield 81%, m.p. 105–109 °C.^{1}H NMR (DMSO-d_6) δ 0.91 (t, 3H, $-$CH$_3$, $J = 7.3$ Hz), 1.33–1.42 (m, 2H, $-$CH$_2-$), 1.56–1.65 (m, 2H, $-$CH$_2-$), 2.68–2.72 (m, 4H, 2,6-piperazine), 3.28–3.33 (m, 4H, 3,5-piperazine), 3.95 (s, 2H, COCH$_2$N), 4.09 (t, 2H, OCH$_2-$, $J = 6.6$ Hz), 7.06 (d, 2H, ArH,$J = 8.8$ Hz), 7.43 (t, 1H, ArH, $J = 7.7$ Hz), 7.50 (d, 2H, ArH, $J = 9.1$ Hz), 7.65–7.70 (m, 2H, ArH), 8.13 (s, 1H, ArH), 9.85 (s, 1H, NH). ^{13}C NMR (DMSO-d_6) δ 196.07, 153.56, 153.04, 139.55, 136.29, 128.89, 125.98 (q, $J = 3.8$ Hz), 124.90 (q, $J = 270.1$ Hz), 122.76, 122.07, 117.80 (q, $J = 32.1$ Hz), 117.32, 114.08, 63.91, 63.22, 52.09, 46.71, 30.43, 18.43, 13.37.

*4.3.3.4. Butyl (3-{[4-(pyridin-2-yl)piperazin-1-yl]acetyl}phenyl)carbamate (**17c**).* Yellow solid, Yield 83%, m.p. 148–152 °C.^{1}H NMR (DMSO-d_6) δ 0.91 (t, 3H, $-$CH$_3$, $J = 7.3$ Hz), 1.33–1.43 (m, 2H, $-$CH$_2-$), 1.57–1.64 (m, 2H, $-$CH$_2-$), 2.59–2.63 (m, 4H, 2,6-piperazine), 3.47–3.51 (m, 4H, 3,5-piperazine), 3.87 (s, 2H, COCH$_2$N), 4.09 (t, 2H, OCH$_2-$, $J = 6.6$ Hz), 6.62 (dd, 1H, ArH, $J = 7.1$ Hz, $J = 4.8$ Hz), 6.81 (d, 1H, ArH, $J = 8.2$ Hz), 7.42 (t, 1H, ArH, $J = 7.8$ Hz), 7.51 (ddd, 1H, ArH, $J = 8.7$ Hz, $J = 7.1$ Hz, $J = 2.1$ Hz), 7.65 (d, 1H, ArH, $J = 7.8$ Hz), 7.70 (d, 1H, ArH, $J = 8.2$ Hz), 8.09–8.13 (m, 2H, ArH), 9.83 (s, 1H, NH). ^{13}C NMR (DMSO-d_6) δ 196.44, 158.99, 153.66, 147.54, 139.66, 127.48, 136.41, 129.06, 122.71, 122.21, 117.28, 112.95, 107.04, 64.03, 63.65, 52.44, 44.54, 30.55, 18.60, 13.60.

*4.3.3.5. Propyl (3-{[4-(pyrimidin-2-yl)piperazin-1-yl]acetyl}phenyl) carbamate (**20c**).* White solid, Yield 78%, m.p. 98 °C.^{1}H NMR (DMSO-d_6) δ 0.93 (t, 3H, $-$CH$_3$, $J = 7.3$ Hz), 1.60–1.70 (m, 2H, $-$CH$_2$-), 2.53–2.58 (m, 4H, 2,6-piperazine), 3.72–3.77 (m, 4H, 3,5-piperazine), 3.86 (s, 2H, COCH$_2$N), 4.05 (t, 2H, OCH$_2-$, $J = 6.6$ Hz), 6.61 (t, 1H, ArH, $J = 4.8$ Hz), 7.42 (t, 1H, ArH, $J = 8.1$ Hz), 7.63–7.72 (m, 2H, ArH), 8.12 (s, 1H, ArH), 8.35 (d, 2H, ArH, $J = 4.8$ Hz), 9.84 (s, 1H, NH). ^{13}C NMR (DMSO-d_6) δ 196.41, 161.13, 157.81, 153.62, 139.58, 136.38, 128.95, 122.69, 122.12, 117.34, 109.98, 65.77, 63.56, 52.34, 43.16, 21.79, 10.14.

*4.3.3.6. Butyl (3-{[4-(pyrimidin-2-yl)piperazin-1-yl]acetyl}phenyl) carbamate (**21c**).* White solid, Yield 79%, m.p. 135–136 °C.^{1}H NMR (DMSO-d_6) δ 0.90 (t, 3H, $-$CH$_3$, $J = 7.3$ Hz), 1.33–1.43 (m, 2H, $-$CH$_2-$), 1.56–1.66 (m, 2H, $-$CH$_2-$), 2.53–2.58 (m, 4H, 2,6-piperazine), 3.72–3.78 (m, 4H, 3,5-piperazine), 3.85 (s, 2H, COCH$_2$N), 4.08 (t, 2H, OCH$_2-$, $J = 6.6$ Hz), 6.60 (t, 1H, ArH,

$J = 4.8$ Hz), 7.41 (t, 1H, ArH, $J = 7.9$ Hz), 7.64–7.71 (m, 2H, ArH), 8.11 (s, 1H, ArH), 8.34 (d, 2H, ArH, $J = 4.8$ Hz), 9.83 (s, 1H, NH). ^{13}C NMR (DMSO-d_6) δ 196.41, 161.13, 157.79, 153.60, 139.58, 136.38, 128.95, 122.68, 122.12, 117.34, 109.98, 63.96, 63.56, 52.34, 43.17, 30.47, 18.50, 13.46.

*4.3.4. General procedure for preparation of alkyl {2-/3-[1-hydroxy-2-(4-arylpiperazin-1-yl)ethyl] phenyl}carbamates (**14–21**)*

Solid sodium borohydride (0.30 g; 8.0 mmol) was added in small portions to a solution of the appropriate alkyl {2-/3-[(4-arylpiperazin-1-yl)acetyl]phenyl}carbamate (4.0 mmol) in hot methanol (50 mL), and then the mixture was refluxed for 1 h. The solvent was removed under reduced pressure, and the residue was treated with distilled water (100 mL) and chloroform (100 mL). The organic phase was washed with additional water, dried over anhydrous sodium sulfate and solvent removed under reduced pressure to give a crude product, which was recrystallized from acetone.

*4.3.4.1. Ethyl (2-{2-[4-(2-fluorophenyl)piperazin-1-yl]-1-hydroxyethyl} phenyl)carbamate (**14**)*. White solid, Yield 21%, m.p. 128–131 °C; IR (cm^{-1}): 3449 (ν NH), 2936 (ν_{as} CH_2), 2831 (ν_s CH_2), 1705 (ν C=O and δ NH), 1502 (ν CN), 1234 (ν_{as} COC), 1056 (ν_s CO); ^{1}H NMR (DMSO-d_6) δ 1.18 (t, 3H, $-CH_3$, $J = 7.0$ Hz), 2.54–2.70 (m, 6H, 2,6-piperazine; $-CH_2N$), 3.00–3.05 (m, 4H, 3,5-piperazine), 4.09 (q, 2H, OCH_2-, $J = 7.0$ Hz), 4.89–4.95 (m, 1H, $-CH-$), 5.51 (d, 1H, OH, $J = 3.7$ Hz), 6.93–7.22 (m, 6H, ArH), 7.42 (d, 1H, ArH, $J = 7.7$ Hz), 7.62 (d, 1H, ArH, $J = 7.7$ Hz), 9.83 (s, 1H, NH).^{13}C NMR (DMSO-d_6) δ 154.80 (d, $J = 242.8$ Hz), 153.63, 139.65 (d, $J = 8.4$ Hz), 135.57, 135.55, 126.90, 126.32, 124.61 (d, $J = 3.0$ Hz), 123.42, 122.06 (d, $J = 7.6$ Hz), 121.98, 118.95 (d, $J = 2.3$ Hz), 115.77 (d, $J = 20.5$ Hz), 67.54, 65.60, 60.01, 53.32, 49.73 (d, $J = 3.1$ Hz), 14.39. HR-MS (Orbitrap): $C_{21}H_{27}FN_3O_3$ $[M + H]^+$ calculated 388.2031 *m/z*, found 388.2038 *m/z*.

*4.3.4.2. Butyl (3-{2-[4-(4-fluorophenyl)piperazin-1-yl]-1-hydroxyethyl} phenyl)carbamate (**15**)*. White solid, Yield 56%, m.p. 124–127 °C; IR (cm^{-1}): 3311 (ν NH), (ν_{as} CH_2) 2959, 2824 (ν_s CH_2), 1724 (ν C=O and δ NH), 1507 (ν CN), 1217 (ν_{as} COC), 1073 (ν_s CO); ^{1}H NMR (DMSO-d_6) δ 0.91 (t, 3H, $-CH_3$, $J = 7.3$ Hz), 1.33–1.43 (m, 2H, $-CH_2-$), 1.56–1.64 (m, 2H, $-CH_2-$), 2.36–2.53 (m, 2H, CH_2N), 2.63–2.67 (m, 4H, 2,6-piperazine), 3.07–3.12 (m, 4H, 3,5-piperazine), 4.07 (t, 2H, OCH_2-, $J = 6.6$ Hz), 4.66–4.72 (m, 1H, $-CH-$), 5.05 (d, 1H, OH, $J = 3.7$ Hz), 6.93–7.06 (m, 5H, ArH), 7.20 (t, 1H, ArH, $J = 8.1$ Hz), 7.33 (d, 1H, ArH, $J = 8.1$ Hz), 7.51 (s, 1H, ArH), 9.57 (s, 1H, NH). ^{13}C NMR (DMSO-d_6) δ 155.83 (d, $J = 235.0$ Hz), 153.57, 147.91 (d, $J = 3.5$ Hz), 145.24, 138.85, 128.08, 120.02, 116.90 (d, $J = 7.6$ Hz), 116.82, 115.99, 115.09 (d, $J = 21.4$ Hz), 69.88, 66.13, 63.66, 53.00, 48.91, 30.52, 18.49, 13.45. HR-MS (Orbitrap): $C_{23}H_{31}FN_3O_3$ $[M + H]^+$ calculated 416.2344 *m/z*, found 416.2353 *m/z*.

*4.3.4.3. Butyl [3-(1-hydroxy-2-{4-[4-(trifluoromethyl)phenyl]piperazin-1-yl}ethyl)phenyl]carbamate (**16**)*. White solid, Yield 84%, m.p. 130–133 °C; IR (cm^{-1}): 3297 (ν NH), 2959 (ν_{as} CH_2), 2823 (ν_s CH_2), 1698 (ν C=O and δ NH), 1553 (ν CN), 1234 (ν_{as} COC), 1068 (ν_s CO); ^{1}H NMR (DMSO-d_6) δ 0.91 (t, 3H, $-CH_3$, $J = 7.3$ Hz), 1.33–1.42 (m, 2H, $-CH_2-$), 1.56–1.64 (m, 2H, $-CH_2-$), 2.37–2.53 (m, 2H, CH_2N), 2.59–2.65 (m, 4H, 2,6-piperazine), 3.25–3.29 (m, 4H, 3,5-piperazine), 4.07 (t, 2H, OCH_2-, $J = 6.6$ Hz), 4.67–4.72 (m, 1H, $-CH-$), 5.08 (d, 1H, OH, $J = 3.7$ Hz), 6.98 (d, 1H, ArH, $J = 7.7$ Hz), 7.06 (d, 2H, ArH,$J = 8.8$ Hz), 7.24 (t, 1H, ArH, $J = 7.7$ Hz), 7.32 (d, 1H, ArH, $J = 7.7$ Hz), 7.49 (d, 2H, ArH, $J = 8.8$ Hz), 7.52 (s, 1H, ArH), 9.57 (s, 1H, NH). ^{13}C NMR (DMSO-d_6) δ 153.53, 153.18, 145.15, 138.81, 128.02, 125.95 (q, $J = 3.8$ Hz), 124.88 (q, $J = 270.1$ Hz), 119.98, 117.61 (q, $J = 32.1$ Hz), 116.78, 116.02, 113.92, 69.89, 65.98, 63.61, 52.67, 46.90, 30.49, 18.43, 13.39. HR-MS (Orbitrap): $C_{24}H_{31}F_3N_3O_3$ $[M + H]^+$ calculated 466.2312 *m/z*, found 466.2319 *m/z*.

*4.3.4.4. Butyl (3-{1-hydroxy-2-[4-(pyridin-2-yl)piperazin-1-yl]ethyl} phenyl)carbamate (**17**)*. White solid, Yield 78%, m.p. 112–144 °C; IR (cm^{-1}): 3320 (ν NH), 2959 (ν_{as} CH_2), 2808 (ν_s CH_2), 1699 (ν C=O and δ NH), 1542 (ν CN), 1227 (ν_{as} COC), 1074 (ν_s CO); ^{1}H NMR (DMSO-d_6) δ 0.91 (t, 3H, $-CH_3$, $J = 7.3$ Hz), 1.33–1.42 (m, 2H, $-CH_2-$), 1.56–1.63 (m, 2H, $-CH_2-$), 2.37–2.54 (m, 2H, CH_2N), 2.54–2.59 (m, 4H, 2,6-piperazine), 3.44–3.48 (m, 4H, 3,5-piperazine), 4.07 (t, 2H, OCH_2-, $J = 6.6$ Hz), 4.67–4.72 (m, 1H, $-CH-$), 5.05 (d, 1H, OH, $J = 3.7$ Hz), 6.62 (dd, 1H, ArH, $J = 6.9$ Hz, $J = 5.0$ Hz), 6.80 (d, 1H, ArH, $J = 8.7$ Hz), 6.98 (d, 1H, ArH, $J = 7.3$ Hz), 7.20 (t, 1H, ArH, $J = 7.8$ Hz), 7.32 (d, 1H, ArH, $J = 8.2$ Hz), 7.49–7.53 (m, 2H, ArH), 8.09–8.11 (m, 1H, ArH), 9.56 (s, 1H, NH). ^{13}C NMR (DMSO-d_6) δ 159.11, 153.64, 147.54, 145.37, 138.95, 137.44, 128.23, 120.09, 116.77, 115.98, 112.90, 107.04, 69.92, 66.41, 63.75, 52.94, 44.68, 30.62, 18.62, 13.62. HR-MS (Orbitrap): $C_{22}H_{31}N_4O_3$ $[M + H]^+$ calculated 399.2391 *m/z*, found 399.2402 *m/z*.

*4.3.4.5. Propyl (3-{1-hydroxy-2-[4-(pyrimidin-2-yl)piperazin-1-yl]ethyl} phenyl)carbamate (**20**)*. White solid, Yield 74%, m.p. 113–115 °C; IR (cm^{-1}): 3254 (ν NH), 2963 (ν_{as} CH_2), 2812 (ν_s CH_2), 1704 (ν C=O and δ NH), 1546 (ν CN), 1229 (ν_{as} COC), 1068 (ν_s CO); ^{1}H NMR (DMSO-d_6) δ 0.92 (t, 3H, $-CH_3$, $J = 7.3$ Hz), 1.57–1.67 (m, 2H, $-CH_2-$), 2.36–2.44 (m, 2H, CH_2N), 2.53–2.57 (m, 4H, 2,6-piperazine), 3.70–3.75 (m, 4H, 3,5-piperazine), 4.01 (t, 2H, OCH_2-, $J = 6.6$ Hz), 4.67–4.72 (m, 1H, $-CH-$), 5.05 (d, 1H, OH, $J = 3.7$ Hz), 6.59 (t, 1H, ArH, $J = 4.8$ Hz), 6.96 (d, 1H, ArH, $J = 7.3$ Hz), 7.19 (t, 1H, ArH, $J = 7.7$ Hz), 7.32 (d, 1H, ArH, $J = 7.9$ Hz), 7.49 (s, 1H, ArH), 8.30–8.37 (m, 2H, ArH), 9.56 (s, 1H, NH). ^{13}C NMR (DMSO-d_6) δ 161.20, 157.77, 153.60, 145.21, 138.87, 128.11, 120.04, 116.81, 116.02, 109.92, 69.83, 66.25, 65.49, 52.85, 43.31, 21.84, 10.16. HR-MS (Orbitrap): $C_{20}H_{28}N_5O_3$ $[M + H]^+$ calculated 386.2187 *m/z*, found 386.2199 *m/z*.

*4.3.4.6. Butyl (3-{1-hydroxy-2-[4-(pyrimidin-2-yl)piperazin-1-yl]ethyl} phenyl)carbamate (**21**)*. White solid, Yield 84%, m.p. 89–90 °C; IR (cm^{-1}): 3274 (ν NH), 2924 (ν_{as} CH_2), 2854 (ν_s CH_2), 1703 (ν C=O and δ NH), 1544 (ν CN), 1221 (ν_{as} COC), 1068 (ν_s CO); ^{1}H NMR (DMSO-d_6) δ 0.90 (t, 3H, $-CH_3$, $J = 7.3$ Hz), 1.33–1.42 (m, 2H, $-CH_2-$), 1.55–1.63 (m, 2H, $-CH_2-$), 2.37–2.50 (m, 2H, CH_2N), 2.53–2.67 (m, 4H, 2,6-piperazine), 3.68–3.76 (m, 4H, 3,5-piperazine), 4.06 (t, 2H, OCH_2-, $J = 6.6$ Hz), 4.68–4.72 (m, 1H, $-CH-$), 5.05 (d, 1H, OH, $J = 3.7$ Hz), 6.59 (t, 1H, ArH, $J = 4.8$ Hz), 6.96 (d, 1H, ArH, $J = 7.3$ Hz), 7.19 (t, 1H, ArH, $J = 7.7$ Hz), 7.32 (d, 1H, ArH, $J = 7.9$ Hz), 7.49 (s, 1H, ArH), 8.33–8.40 (m, 2H, ArH), 9.54 (s, 1H, NH). ^{13}C NMR (DMSO-d_6) δ 161.19, 157.76, 153.57, 145.20, 138.87, 128.10, 120.02, 116.79, 116.00, 109.90, 69.82, 66.24, 63.66, 52.84, 43.29, 30.53, 18.50, 13.46. HR-MS (Orbitrap): $C_{21}H_{30}N_5O_3$ $[M + H]^+$ calculated 400.2343 *m/z*, found 400.2351 *m/z*.

4.4. Synthesis of compounds 22 and 23 (Scheme 2)

Synthesis, intermediates and compound target 4-[3-({4-[(buthoxycarbonyl)amino]benzoyl}oxy)-2-hydroxypropyl]-1-phenylpiperazin-1-ium chloride (**22**) were described recently [31].

4.4.1. General procedure for preparation of 1-(3-{4-[(propoxycarbonyl) amino]benzoyloxy}-2-hydroxypropyl)-4-phenylpiperazin-1-ium chloride (23)

A mixture of oxiran-2-ylmethyl 4-[(propoxycarbonyl)amino] benzoate (**23a**) [29] (0.2 mol) and 1-(4-phenyl)piperazine (0.2 mol) in *i*-PrOH (150 mL) was heated at 80 °C for 4 h. The solvent was evaporated under reduced pressure, and the residing oil was dissolved in Et_2O. The solution of the base was converted to its chloride salt by addition of ethereal HCl. The piperazine salt was collected by filtration and recrystallized from *i*-PrOH to give white crystals.

*4.4.1.1. 1-(2-hydroxy-3-{4-[(propoxycarbonyl)amino]benzoyloxy} propyl)-4-phenylpiperazin-1-ium chloride (**23**)*. White solid; Yield 59%;

m.p. 189–191 °C; FT-IR (ZnSe ATR, cm^{-1}): 3375 (ν NH), 3256 (ν OH), 2969 (ν CH), 2565 (ν NH^+), 1734 (ν C═O), 1702 (ν NHC = O), 1598 (ν_{ring} C═C); ^1H NMR (DMSO-d_6), δ: 10.68 (s, 1H, $-NH^+-$), 10.13 (s, 1H, −NH), 7.98 (d, $J = 8.7$, 2H, ArH), 7.63 (d, $J = 8.7$, 2H, ArH), 7.30–7.22 (m, 2H, ArH-N_{pip}), 7.02–6.98 (m, 2H, ArH-N_{pip}), 6.89–6.82 (m, 1H, ArH-N_{pip}), 6.07 (s, 1H, −OH), 4.50–4.42 (m, 1H, −CH−), 4.23–4.21 (m, 2H, $-COOCH_2-$), 4.06 (t, $J = 6.7$, 2H, OCH_2-), 3.83–3.61 (m, 4H, H_{pip}), 3.38–3.09 (m, 6H, H_{pip} + $-CH_2$-N_{pip}), 1.73–1.56 (m, 2H, $-CH_2-$), 0.93 (t, $J = 7.4$, 3H, $-CH_3$); ^{13}C NMR (50 MHz, DMSO-d_6), δ: 165.0, 153.2, 149.0, 143.7, 130.1, 128.7, 122.5, 120.2, 117.0, 115.9, 65.8, 65.5, 63.3, 58.9, 52.2, 51.2, 45.6, 21.7, 9.8; HR-MS (Orbitrap): $C_{24}H_{31}N_3O_5$[*M-H*]$^-$calculated 440.2191 *m/z*, found 440.2199 *m/z*.

4.5. Bioassays

4.5.1. Reagents

Vemurafenib was used as a positive control. Stock solution of Vemurafenib (10 mM) and compounds of Table 1 (5 mM) were prepared in DMSO, aliquoted and preserved at −20 °C.

Primary antibodies to detect ERK total (1/2000) and pERK (T202-Y204, 1/1000) were purchased from Cell Signaling and prepared according to manufacturer specifications in TBS buffer (20 mM Tris pH 7,4, 0,9% NaCl) supplemented with 0,1% Tween-20 and 5% BSA (bovine serum albumin). Secondary antibodies conjugated to near-infrared fluorochromes (IRD, 1/30.000) were from Li-COR and prepared in TBS 0,1% Tween-20 and 3% fatty free milk as recommended by the manufacturer.

MTT reagent (3-(4,5-Dimethyl-2-thiazolyl)-2,5-diphenyl-2H-tetrazolium bromide, Sigma Aldrich) was prepared freshly according to the manufacturer instructions, as described elsewhere [51].

4.5.2. Cell culture

Lu1205 melanoma cell line was a generous gift of Dr. Pablo Bergami (Universidad de Maimónides) and was cultured in DMEM (Gibco) supplemented with 10% of fetal bovine serum (Natocor) at 37 °C in humidified atmosphere with 5% CO_2, as described [52,53].

4.5.3. In-cell western blot (ICW)

Lu1205 cells were cultured in complete medium in 96-well plates at a density of 5.000 cells/well until 80–90% of confluence (48–72 h). Then the medium was replaced by fresh medium containing the testing compound at 1 and 10 µM and cultured for 2 h at 37 °C. ICW was performed according to standard protocols provided by Li-COR. Briefly, after the treatment, cells were fixed with ice-cold methanol (-20 °C) for 20 min and washed 3 times with PBS. Then each well was blocked with PBS 3% fatty free milk and 0,1% Tween-20 for 2 h and washed again for 5 min 5 times with PBS 0,1% Tween-20. Next, cells were incubated ON at 4 °C with a mix of primary antibodies anti-pERK (1/400) and anti-tubulin (1/800) prepared in PBS 5% BSA and 0,1% Tween-20. Secondary antibodies R800 and M680 prepared in PBS 3% fatty free milk and 0,1% Tween-20 (Li-COR, 1/1200) were incubated 1 h at room temperature. Plate was washed, dried and immediately scanned with Oddyssey Clx scanner. Images were analyzed with Image Studio software.

4.5.4. Western blot

Western blot experiments were performed essentially as described Campos et al [52]. Lu1205 cells were seeded in 12-well plates at a density of 40.000 cells/well for 72 h. Then, the medium was replaced by fresh medium supplemented with the compounds of Table 1 at the final concentration of 1 and 10 µM and incubated 2 additional hours in the culture heater. Next, medium was discarded and cells were washed with ice-cold PBS and scraped into lysis buffer containing 20 mM Tris-HCl (pH 7.4), 1 mM EDTA, 150 mM NaCl, 1% Triton X-100, 1 mM ß-mercaptoethanol, 1 mM Na_3VO_4, and 1:2 protease inhibitor cocktail (Roche). Lysates were incubated on ice for 1 h and centrifuged at 10.000 *xg* for 15 min. Proteins (30 µg) were separated by SDS-PAGE and blotted onto nitrocellulose. Membranes were blocked 1 h with TBS 0,1% Tween-20 and 3% fatty free milk, and incubated ON at 4 °C with specific primary antibodies as indicated. Inmunopositive bands were detected with appropriate secondary antibodies (IRD, Li-COR, 1/30.000) incubated 1 h at room temperature. Membranes were scanned in Oddyssey Clx and images analyzed with the software Image Studio 5.2. Results correspond to three independent experiments.

4.5.5. Cell viability assay

Lu1205 cells were cultured in 96-well plates at a density of 5.000 cells/well. The next day, culture medium was replaced by fresh medium containing compounds of Table 1 at the final concentration of 1 and 10 µM or control medium containing equal amount of DMSO and cultured for 72 h. The experiment was performed in six replicates for each concentration and each compound. MTT reagent was prepared freshly for each experiment. Briefly, MTT was dissolved in PBS (phosphate saline buffer) 5 mg/mL, vortexed 15′ and sonicated 2′ for five times. Then it was centrifuged at 12.000 xg, 4 °C for 10′ and the supernatant separated. Finally, MTT was diluted at 0,5 mg/mL in DMEM serum free and conserved at 4 °C for each experiment.

After addition of MTT reagent diluted in DMEM serum free cells were incubated three additional hours. Formazan was detected by reading the absorbance at 540 nm (Epoch). Average absorbance of each treatment (six replicates) was normalized with average absorbance of the respective control. Results correspond to three independent experiments.

4.5.6. Statistics

One way-ANOVA analyses and Tukey's post-test were used to determine the significance of western blot and cell viability bioassays.

4.6. Molecular modelling

4.6.1. Virtual screening

All the PDB files were downloaded from the protein data bank. In these structures BRAF is found as a dimmer (i.e. chain A, B) which is the assembly needed for normal Ras-dependent RAF kinase activation. Since the ATP-binding site is far away from the dimmer interface, only chain A from each structure was kept. Then, the monomers were structurally aligned by the protein backbone atoms, hydrogen atoms were added and the X-ray models were split into receptor, co-factors, water molecules and ligands which were saved separately.

Receptors and ligands were prepared for docking (i.e. PDB to PDBQT conversion) by using python scripts provided with the MGL Tools installation [21]. All docking calculations were performed with AutoDock4 program [21].

A single docking grid box was defined on the structurally aligned receptors in such a way that all the crystallographic ligands remain roughly in the box center. Default settings were used for other grid parameters.

Default GA search settings were used except for the number of poses generated that was set to 50 in the docking parameter file (i.e. ga_run = 50).

4.6.2. Computational details

4.6.2.1. MD simulations. We take the geometries obtained from the docking analysis and we soaked them in boxes of explicit water using the TIP3P model [54] and then were subjected to MD simulations. Such simulations were carried out by using the Amber software package [37] using periodic boundary conditions and cubic simulation cells. In these simulations we use the Particle Mesh Ewald method (PME) [55] with a grid spacing of 1.2 Å, a spline interpolation order of 4 Å and a real space direct sum cutoff of 10 Å. In order to obtain an integration time step of 2 fs, we applied the SHAKE algorithm. All the simulations were performed at 310 K temperature and three MD simulations of 30 ns were conducted for each system under different starting velocity distribution functions. Thus, we obtained a total of 90 ns of simulation for each complex. The NPT ensemble was employed using Berendsen coupling to a baro/thermostat (target pressure 1 atm, relaxation time 0.1 ps). Post MD analysis was performed by using the program PTRAJ.

4.6.2.2. Quantum calculations setup. From the MD simulations we constructed reduced 3D model systems including the tested compounds and the main residues at the BRAF binding site. We only included in the different reduced models those side chains of the binding site possessing a $|\Delta G|$ value higher than 1.0 kcal/mol in the per residue analysis, together with each inhibitor.

4.6.2.3. QTAIM calculations. For the QTAIM analysis [56] we use the reduced models as input data, which was performed with the help of Multiwfn software [57]. We employed the Gaussian 16 package [58,59] for the computations and the calculations were carried out by using the B3LYP functional with dispersion correction (B3LYP-D) and 6-31G(d) as basis set. These calculations were selected considering the extension of the system in study because they ensures a reasonable compromise between the wave function quality required to obtain reliable values of the derivatives of $\rho(r)$ and the computation capability available [60].

Acknowledgements

This work was supported by grants from INC (Instituto Nacional del Cáncer-Argentina) to R.D.E., ANPCyT-Argentina PICT 2378-2014 to S.E.A. and CONICET, Argentina PIP916-2015 to S.E.A. Grants from Universidad Nacional de San Luis (UNSL-Argentina) partially supported this work. Dr. Ludmila Campos is a postdoctoral fellowship of CONICET-Argentina. This work was also partially supported by the Ministry of Education of the Czech Republic (LO1305) and by the Slovak Research and Development Agency (APVV-17-0373 and APVV-17-0318).

Appendix A. Supplementary material

Supplementary data to this article can be found online at https://doi.org/10.1016/j.bioorg.2019.103125.

References

[1] M. Dankner, A.A.N. Rose, S. Rajkumar, P.M. Siegel, I.R. Watson, Classifying BRAF alterations in cancer: new rational therapeutic strategies for actionable mutations, Oncogene 37 (2018) 3183–3199, https://doi.org/10.1038/s41388-018-0171-x [pii].

[2] Cancer, I. A. f. R. i. https://www.iarc.fr/, 2018.

[3] P.T. Wan, et al., Mechanism of activation of the RAF-ERK signaling pathway by oncogenic mutations of B-RAF, Cell 116 (2004) 855–867 doi:S0092867404002156 [pii].

[4] P.B. Chapman, et al., Improved survival with vemurafenib in melanoma with BRAF V600E mutation, N. Engl. J. Med. 364 (2011) 2507–2516, https://doi.org/10.1056/NEJMoa1103782.

[5] A. Hauschild, et al., Dabrafenib in BRAF-mutated metastatic melanoma: a multicentre, open-label, phase 3 randomised controlled trial, Lancet 380 (2012) 358–365, https://doi.org/10.1016/S0140-6736(12)60868-X S0140-6736(12)60868-X [pii].

[6] G.V. Long, et al., Dabrafenib and trametinib versus dabrafenib and placebo for Val600 BRAF-mutant melanoma: a multicentre, double-blind, phase 3 randomised controlled trial, Lancet 386 (2015) 444–451, https://doi.org/10.1016/S0140-6736(15)60898-4 S0140-6736(15)60898-4 [pii].

[7] J. Larkin, et al., Combined vemurafenib and cobimetinib in BRAF-mutated melanoma, N. Engl. J. Med. 371 (2014) 1867–1876, https://doi.org/10.1056/NEJMoa1408868.

[8] S. Kakadia, et al., Mechanisms of resistance to BRAF and MEK inhibitors and clinical update of US Food and Drug Administration-approved targeted therapy in advanced melanoma, Onco Targets Ther 11 (2018) 7095–7107, https://doi.org/10.2147/OTT.S182721ott-11-7095[pii].

[9] H. Shi, et al., Acquired resistance and clonal evolution in melanoma during BRAF inhibitor therapy, Cancer Discov 4 (2014) 80–93, https://doi.org/10.1158/2159-8290.CD-13-0642.

[10] C. Montagut, et al., Elevated CRAF as a potential mechanism of acquired resistance to BRAF inhibition in melanoma, Cancer Res. 68 (2008) 4853–4861, https://doi.org/10.1158/0008-5472.CAN-07-6787 68/12/4853 [pii].

[11] S.J. Heidorn, et al., Kinase-dead BRAF and oncogenic RAS cooperate to drive tumor progression through CRAF, Cell 140 (2010) 209–221, https://doi.org/10.1016/j.cell.2009.12.040 S0092-8674(09)01626-2 [pii].

[12] H. Shi, et al., Melanoma whole-exome sequencing identifies (V600E)B-RAF amplification-mediated acquired B-RAF inhibitor resistance, Nat. Commun. 3 (2012) 724, https://doi.org/10.1038/ncomms1727 ncomms1727 [pii].

[13] P.I. Poulikakos, C. Zhang, G. Bollag, K.M. Shokat, N. Rosen, RAF inhibitors transactivate RAF dimers and ERK signalling in cells with wild-type BRAF, Nature 464 (2010) 427–430, https://doi.org/10.1038/nature08902 nature08902 [pii].

[14] F. Su, et al., RAS mutations in cutaneous squamous-cell carcinomas in patients treated with BRAF inhibitors, N. Engl. J. Med. 366 (2012) 207–215, https://doi.org/10.1056/NEJMoa1105358.

[15] R. Roskoski Jr., Classification of small molecule protein kinase inhibitors based upon the structures of their drug-enzyme complexes, Pharmacol. Res. 103 (2016) 26–48, https://doi.org/10.1016/j.phrs.2015.10.021 S1043-6618(15)30129-8 [pii].

[16] D.K. Treiber, N.P. Shah, Ins and outs of kinase DFG motifs, Chem. Biol. 20 (2013) 745–746, https://doi.org/10.1016/j.chembiol.2013.06.001 S1074-5521(13)00214-7 [pii].

[17] B. Agianian, E. Gavathiotis, Current insights of BRAF inhibitors in cancer, J. Med. Chem. 61 (2018) 5775–5793, https://doi.org/10.1021/acs.jmedchem.7b01306.

[18] S. Wenglowsky, et al., Pyrazolopyridine inhibitors of B-Raf(V600E). Part 4: rational design and kinase selectivity profile of cell potent type II inhibitors, Bioorg. Med. Chem. Lett. 22 (2012) 6237–6241, https://doi.org/10.1016/j.bmcl.2012.08.007 S0960-894X(12)00996-1 [pii].

[19] W. Zheng, S.R. Johnson, in: Chemoinformatics Approaches to Virtual Screening (ed The Royal Society of Chemistry), 2008, pp. 268–294.

[20] E.J. Bjerrum, Machine learning optimization of cross docking accuracy, Comput. Biol. Chem. 62 (2016) 133–144, https://doi.org/10.1016/j.compbiolchem.2016.04.005 S1476-9271(16)30021-4 [pii].

[21] G.M. Morris, et al., AutoDock4 and AutoDockTools4: automated docking with selective receptor flexibility, J. Comput. Chem. 30 (2009) 2785–2791, https://doi.org/10.1002/jcc.21256.

[22] M.M. Mysinger, M. Carchia, J.J. Irwin, B.K. Shoichet, Directory of useful decoys, enhanced (DUD-E): better ligands and decoys for better benchmarking, J. Med. Chem. 55 (2012) 6582–6594, https://doi.org/10.1021/jm300687e.

[23] N.M. O'Boyle, et al., Open Babel: an open chemical toolbox, J Cheminform 3 (2011) 33, https://doi.org/10.1186/1758-2946-3-33 1758-2946-3-33 [pii].

[24] J. Kos, et al., Synthesis and antimycobacterial properties of ring-substituted 6-hydroxynaphthalene-2-carboxanilides, Bioorg. Med. Chem. 23 (2015) 2035–2043, https://doi.org/10.1016/j.bmc.2015.03.018 S0968-0896(15)00185-6 [pii].

[25] T. Gonec, et al., Halogenated 1-hydroxynaphthalene-2-carboxanilides affecting photosynthetic electron transport in photosystem II, Molecules 22 (2017), https://doi.org/10.3390/molecules22101709 molecules22101709 [pii].

[26] T. Gonec, et al., Antibacterial and herbicidal activity of ring-substituted 2-hydroxynaphthalene-1-carboxanilides, Molecules 18 (2013) 9397–9419, https://doi.org/10.3390/molecules18089397 molecules18089397 [pii].

[27] T. Tomasic, et al., Discovery of 4,5,6,7-tetrahydrobenzo[1,2-d]thiazoles as novel DNA gyrase inhibitors targeting the ATP-binding site, J. Med. Chem. 58 (2015) 5501–5521, https://doi.org/10.1021/acs.jmedchem.5b00489.

[28] T. Tomasic, et al., Design, synthesis and biological evaluation of 4,5-dibromo-N-(thiazol-2-yl)-1H-pyrrole-2-carboxamide derivatives as novel DNA gyrase inhibitors, Bioorg. Med. Chem. 25 (2017) 338–349, https://doi.org/10.1016/j.bmc.2016.10.038 S0968-0896(16)31093-8 [pii].

[29] M. Gjorgjieva, et al., Discovery of Benzothiazole scaffold-based DNA gyrase B inhibitors, J. Med. Chem. 59 (2016) 8941–8954, https://doi.org/10.1021/acs.jmedchem.6b00864.

[30] N. Zidar, et al., N-Phenyl-4,5-dibromopyrrolamides and N-phenylindolamides as ATP competitive DNA gyrase B inhibitors: design, synthesis, and evaluation, J. Med. Chem. 58 (2015) 6179–6194, https://doi.org/10.1021/acs.jmedchem.5b00775.

[31] J. Tengler, et al., Synthesis and biological evaluation of 2-hydroxy-3-[(2-aryloxyethyl)amino]propyl 4-[(alkoxycarbonyl)amino]benzoates, Sci. World J. 2013 (2013) 274570, https://doi.org/10.1155/2013/274570.

[32] P. Marvanova, et al., Synthesis and characterization of new 3-(4-arylpiperazin-1-yl)-2-hydroxypropyl 4-propoxybenzoates and their hydrochloride salts, Molecules 21 (2016), https://doi.org/10.3390/molecules21060707 molecules21060707 [pii].

[33] I. Wortzel, R. Seger, The ERK cascade: distinct functions within various subcellular organelles, Genes. Cancer 2 (2011) 195–209, https://doi.org/10.1177/1947601911407328 10.1177_1947601911407328 [pii].

[34] J. Tsai, et al., Discovery of a selective inhibitor of oncogenic B-Raf kinase with potent antimelanoma activity, Proc. Natl. Acad Sci. U.S.A. 105 (2008) 3041–3046, https://doi.org/10.1073/pnas.0711741105 0711741105 [pii].

[35] R.B. Corcoran, et al., EGFR-mediated re-activation of MAPK signaling contributes to insensitivity of BRAF mutant colorectal cancers to RAF inhibition with vemurafenib, Cancer Discov. 2 (2012) 227–235, https://doi.org/10.1158/2159-8290.CD-11-0341.

[36] J.N. Sondergaard, et al., Differential sensitivity of melanoma cell lines with BRAFV600E mutation to the specific Raf inhibitor PLX4032, J Transl Med 8 (2010) 39, https://doi.org/10.1186/1479-5876-8-39 1479-5876-8-39 [pii].

[37] Amber 2014, 2014.

[38] S.A. Andujar, et al., Searching the “biologically relevant”conformation of dopamine: a computational approach, J. Chem. Inf. Model. 52 (2012) 99–112, https://doi.org/10.1021/ci2004225.

[39] E.L. Angelina, S.A. Andujar, R.D. Tosso, R.D. Enriz, N.M. Peruchena, Non-covalent interactions in receptor-ligand complexes. A study based on the electron charge density, J. Phys. Org. Chem. 27 (2014) 7.
[40] L.J. Gutierrez, et al., New small-size peptides modulators of the exosite of BACE1 obtained from a structure-based design, J. Biomol. Struct. Dyn. 35 (2017) 413–426, https://doi.org/10.1080/07391102.2016.1145143.
[41] J. Parraga, et al., Dopaminergic isoquinolines with hexahydrocyclopenta[ij]-isoquinolines as D2-like selective ligands, Eur. J. Med. Chem. 122 (2016) 27–42, https://doi.org/10.1016/j.ejmech.2016.06.009 S0223-5234(16)30486-X [pii].
[42] J. Parraga, et al., 2,3,9- and 2,3,11-trisubstituted tetrahydroprotoberberines as D2 dopaminergic ligands, Eur. J. Med. Chem. 68 (2013) 150–166, https://doi.org/10.1016/j.ejmech.2013.07.036 S0223-5234(13)00484-4 [pii].
[43] R.D. Tosso, et al., Molecular modeling study of dihydrofolate reductase inhibitors. Molecular dynamics simulations, quantum mechanical calculations, and experimental corroboration, J. Chem. Inf. Model. 53 (2013) 2018–2032, https://doi.org/10.1021/ci400178h.
[44] M. Vettorazzi, et al., An integrative study to identify novel scaffolds for sphingosine kinase 1 inhibitors, Eur. J. Med. Chem. 139 (2017) 461–481, https://doi.org/10.1016/j.ejmech.2017.08.017 S0223-5234(17)30620-7 [pii].
[45] M. Vettorazzi, et al., Theoretical models to predict the inhibitory effect of ligands of sphingosine kinase 1 using QTAIM calculations and hydrogen bond dynamic propensity analysis, J. Comput. Aided Mol. Des. 32 (2018) 781–791, https://doi.org/10.1007/s10822-018-0129-7 10.1007/s10822-018-0129-7 [pii].
[46] S. Wenglowsky, et al., Highly potent and selective 3-N-methylquinazoline-4(3H)-one based inhibitors of B-Raf(V600E) kinase, Bioorg. Med. Chem. Lett. 24 (2014) 1923–1927, https://doi.org/10.1016/j.bmcl.2014.03.007 S0960-894X(14)00223-6 [pii].
[47] W.L.F.A.a.J.I.C. Smith, Quinazolines. Part VIII. Electronic effects in 2-substituted quinazolines, J. Chem. Soc. C 6 (1966).
[48] F. Ishikawa, Y. Watanabe, J. Saegusa, Cyclic guanidines. IX. Synthesis of 2-amino-3,4-dihydroquinazolines as blood platelet aggregation inhibitors, Chem Pharm Bull (Tokyo) 28 (1980) 1357–1364.
[49] R.K. Pandey, S.P. Dagade, M.K. Dongare, P. Kumar, Synthesis of carbamates using Yttria-Zirconia based lewis acid catalyst, Synth. Commun. 33 (2003) 9.
[50] J.L. Garcia Ruano, C. Pedregal, J.H. Rodriguez, Synthesis and conformational analysis of the bioisosteres of oxisuran, Anales de Quimica, Serie C: QuimicaOrganicaiBioquimica 84 (1988) 9.
[51] T. Mosmann, Rapid colorimetric assay for cellular growth and survival: application to proliferation and cytotoxicity assays, J. Immunol. Methods 65 (1983) 55–63 0022-1759(83)90303-4 [pii].
[52] L.S. Campos, et al., Filamin a expression negatively regulates sphingosine-1-phosphate-induced NF-kappaB activation in melanoma cells by inhibition of Akt signaling, Mol. Cell. Biol. 36 (2016) 320–329, https://doi.org/10.1128/MCB.00554-15 MCB.00554-15 [pii].
[53] M.G. Castro, L.E. Campos, Y.I. Rodriguez, S.E. Alvarez, In vitro methods to study the modulation of migration and invasion by sphingosine-1-phosphate, Methods Mol. Biol. 1697 (2018) 117–131, https://doi.org/10.1007/7651_2017_51.
[54] P. Mark, L. Nilsson, Structure and dynamics of the TIP3P, SPC, and SPC/E water models at 298 K, J. Phys. Chem. 105 (2001) 6.
[55] T. Darden, D. York, L. Pedersen, Particle mesh Ewald: An N.log(n) method for Ewald sums in large systems, J. Chem. Phys. 98 (1993) 4.
[56] R.F.W. Bader, Atoms in molecules, Acc. Chem. Res. 18 (1985) 7.
[57] T. Lu, F. Chen, Multiwfn: a multifunctional wavefunction analyzer, J. Comput. Chem. 33 (2012) 580–592, https://doi.org/10.1002/jcc.22885.
[58] Gaussian 09, 2009.
[59] Gaussian 16, 2016.
[60] E.E. Barrera Guisasola, et al., Pentameric models as alternative molecular targets for the design of new antiaggregant agents, Curr. Protein Pept. Sci. 17 (2016) 156–168 CPPS-EPUB-71511 [pii].